Electronic, magnetic, and electric transport properties of Ce_{3}Rh_{4}Sn_{13} and Ce_{3}Co_{4}Sn_{13}: A comparative study

A. Ślebarski, B. D. White, M. Fijałkowski, J. Goraus, J. J. Hamlin, and M. B. Maple

Phys. Rev. B **86**, 205113 — Published 9 November 2012

DOI: 10.1103/PhysRevB.86.205113

Electronic, magnetic, and electric transport properties of $Ce_3Rh_4Sn_{13}$ and $Ce_3Co_4Sn_{13}$: A comparative study

A. Ślebarski*, B. D. White†, M. Fijałkowski*, J. Goraus*, J. J. Hamlin†, and M. B. Maple†
*Institute of Physics, University of Silesia, 40-007 Katowice, Poland
†Department of Physics, University of California, San Diego, La Jolla, California 92093, USA

We present an investigation of the magnetic, thermodynamic, and electric transport properties, and the electronic structure of the strongly correlated compounds $Ce_3Rh_4Sn_{13}$ and $Ce_3Co_4Sn_{13}$. The main goal of this report is to compare the physical properties of both compounds and to explain the abnormal electrical resistivity behavior in $Ce_3Co_4Sn_{13}$ above $\sim$ 160 K, which has not been observed in $Ce_3Rh_4Sn_{13}$. We suggest that a possible local distortion of the trigonal Sn2 prisms around Co occurs in $Ce_3Co_4Sn_{13}$ below $\sim$ 160 K, which could change the electronic structure near the Fermi level, and as a consequence, explain the metallic behavior visible in the resistivity above this temperature. We determined experimentally the hybridization energy Δ between the f-electron and conduction-electron states for both compounds and its influence on the different $\rho(T)$ behaviors under pressure. The complimentary experimental data allowed us to explain the semimetallic properties of both compounds and the transition between semimetallic and metallic behavior in $Ce_3Co_4Sn_{13}$, which is not observed for $Ce_3Rh_4Sn_{13}$.

PACS numbers: 71.27.+a, 72.15.Qm, 71.30+h

I. INTRODUCTION

The series of intermetallic compounds $R_3M_4Sn_{13}$, first reported by Remeika et al.,[1] has been systematically studied, especially for the specimens with M = Co[2–4], Rh[5], and Ir.[2,6] These intermetallic compounds have been the subject of intensive investigations recently for several reasons. (*i*) The ternary $Ce_3M_4Sn_{13}$ stannides crystallize in the cubic $Yb_3M_4Sn_{13}$ structure (space group $Pm\bar{3}n$), which is closely related to that of the skutterudites, which are well known thermoelectric materials. These compounds contain two distinct Sn sites, Sn1 (*2a*) and Sn2 (*24k*). The Sn2 atoms form a $M(Sn2)_6$ trigonal prism which are arranged in a three-dimensional network containing two different cages: one occupied by Ce ($Ce(Sn2)_{12}$) and the other by the Sn1 ($Sn1(Sn2)_{12}$) atoms. X-ray diffraction measurements have suggested the possibility of local vibrations of Sn atoms inside the cage,[7] which can lead to the *rattling* effect responsible for the low phonon thermal conductivities found in filled cage compounds. The efficiency of thermoelectric devices is characterized by the thermoelectric figure-of-merit $ZT = S^2\sigma T/\kappa$, where S is the Seebeck coefficient (or thermopower), σ is the electrical conductivity, and κ is the total thermal conductivity with contributions from electrons and the lattice. The thermopower of $Ce_3Rh_4Sn_{13}$ is weakly temperature dependent and small.[5,7] (*ii*) Heavy fermion compound $Ce_3Ir_4Sn_{13}$ orders antiferromagnetically and demonstrates an intriguing double peak feature in the specific heat at 2.1 and 0.6 K.[6] On the other hand, low-temperature neutron diffraction results[8,9] and specific heat measurements[3,5] show no evidence for long-range magnetic order in either $Ce_3Co_4Sn_{13}$ or $Ce_3Rh_4Sn_{13}$; although there is evidence for two magnetic phase transitions at 1.2 and 2 K in the heat capacity data reported for the Rh-sample.[10] Recently, our theoretical simulation of vacancies at the 2*a* sites revealed, within the virtual crystal approximation (VCA), that the magnetic ground state of $Ce_3Rh_4Sn_{13}$ is very sensitive to the Sn content.[11] Even slight non-homogeneity or nonstoichiometry of the sample can result in different magnetic properties, as is investigated experimentally in this report. (*iii*) An increasing number of Ce based heavy fermion (HF) metals have been shown to display a pronounced deviation from the properties of conventional Landau-Fermi liquids (LFL). In a number of cases, this non-Fermi-liquid (NFL) behavior can be attributed to the proximity to a quantum-critical transition at $T = 0$ between magnetic and nonmagnetic ground states, which can be tuned by varying a control parameter such as pressure (P), magnetic fields (B), or doping.[12] Such zero-temperature quantum critical points (QCP) can drive unusual behavior in thermodynamic properties, as well as in transport over a wide range of temperatures. The previous investigations of $Ce_3Co_4Sn_{13}$ and $Ce_3Rh_4Sn_{13}$ indicated a large increase in C/T at low temperatures. The maximum value of $\sim$ 4 J/(mol-Ce-K^2), obtained at the lowest temperature, would seem to indicate that both compounds are likely very near a magnetic QCP,[3] whereas in applied magnetic fields they show a cross-over from a magnetically correlated state to a single impurity Kondo state.

In this paper, we investigate the thermodynamic and electrical transport properties of $Ce_3Co_4Sn_{13}$ and $Ce_3Rh_4Sn_{13}$ versus magnetic field and external pressure. We found that both compounds are in the metallic state under the maximal pressure of 2.7 GPa and field of 9 T, however, with quite different $\rho(T)$ dependencies. The discussion of the field and pressure dependent $\rho(T)$ data is based on band structure properties. Through comparative studies of $Ce_3Co_4Sn_{13}$ and $Ce_3Rh_4Sn_{13}$, we try to elucidate the nature of magnetic correlations as well as to explain why they are not strong enough to promote long-range order.

II. EXPERIMENTAL DETAILS

Polycrystalline $La_3M_4Sn_{13}$ and $Ce_3M_4Sn_{13}$ samples have been prepared by arc melting the constituent elements on a water cooled copper hearth in a high-purity argon atmosphere with an Al getter. The samples were remelted several times to promote homogeneity and annealed at 870 °C for 12 days. Almost no mass loss ($\leq 0.02\%$) occurred during the melting and annealing process. All samples were carefully examined by x-ray diffraction analysis and found to be single phase with cubic structure (space group $Pm\bar{3}n$). The powder diffraction pattern was measured with a Rigaku-Denki D/MAX RAPID II-R diffractometer (Rigaku Corporation, Tokyo, Japan) with a rotating anode Ag K_α tube (λ =0.5608 Å), an incident beam (002) graphite monochromator, and an image plate in the Debye-Scherrer geometry. Powder diffraction studies below room temperature were performed using a Siemens D5000 high-resolution diffractometer equipped with an Anton Paar He TTK low temperature system.

Stoichiometry and homogeneity were checked by the microprobe technique (scanning microscope JSM-5410) and by XPS analysis. Deviations from the nominal composition were small. Due to our previous *ab initio* calculations, which showed that the magnetic ground state of $Ce_3Rh_4Sn_{13}$ is very sensitive to Sn content, we studied the influence of the Sn-stoichiometry on the thermodynamical properties of $Ce_{14.57}Rh_{20.86}Sn_{64.57}$ (sample #1) and $Ce_{14.28}Rh_{20.37}Sn_{65.36}$ (sample #2).

Electrical resistivity ρ was investigated by a conventional four-point ac technique using a Quantum Design Physical Properties Measurement System (PPMS). Electrical contacts were made with 50 μm-gold wire attached to the samples by spot welding. Electrical resistivity measurements under pressure were performed in a beryllium-copper, piston-

cylinder clamped cell. A 1:1 mixture of n-pentane and isoamyl alcohol in a teflon capsule served as the pressure transmitting medium to ensure hydrostatic conditions during pressurization at room temperature. The local pressure in the sample chamber was inferred from the inductively determined, pressure-dependent superconducting critical temperature of Sn.[16]

Specific heat C was measured in the temperature range $0.6 - 300$ K and in external magnetic fields up to 9 T using a Quantum Design PPMS platform. Specific heat $C(T)$ measurements were carried out on plate-like specimens with masses of about $10 - 15$ mg utilizing a thermal-relaxation method. The dc magnetization M and magnetic susceptibility χ results were obtained using a commercial SQUID magnetometer from 1.8 K to 300 K in magnetic fields up to of 7 T.

XPS spectra were obtained with monochromatized Al K_α radiation at room temperature using a PHI 5700 ESCA spectrometer. The polycrystalline sample was broken under high vacuum of 6×10^{-10} Torr immediately before taking a spectrum. The spectra were calibrated according to Ref. 17, and binding energies were referenced to the Fermi level ($\epsilon_F = 0$).

III. RESULTS AND DISCUSSION: A COMPARATIVE STUDY

A. Magnetic properties

While $Ce_3Ir_4Sn_{13}$ exhibits antiferromagnetic (AFM) ordering[6,18] below 0.6 K, $Ce_3Co_4Sn_{13}$ is paramagnetic[19] down to 0.35 K and $Ce_3Rh_4Sn_{13}$ has been reported to be a paramagnetic[5] or a magnetically ordered[10] compound. Our recent full potential local orbital (FPLO) calculations within the VCA have demonstrated[11] that the vacancies at the $2a$ Sn sites stabilize the magnetic state of $Ce_3Rh_4Sn_{13-\delta}$, where $\delta = 0.1$ and 0.15. In this study, we compare the magnetic data obtained for the almost stoichiometric $Ce_3Rh_4Sn_{13}$ (sample #2) with that obtained for sample #1 with a larger concentration of vacancies at the Sn sites. We also present the results of our magnetic investigations of $Ce_3Co_4Sn_{13}$.[20]

Fig. 1 compares the dc magnetic susceptibility, $\chi(T)$, measured in a magnetic field of 500 Gs, and inverse susceptibility data, $1/\chi$, for $Ce_3Rh_4Sn_{13}$ (samples #1 and #2) and $Ce_3Co_4Sn_{13}$. There is no evidence for frequency dependence in the $\chi(T)$ data (the $\chi_{ac}(T)$ data at $\nu = 160$ Hz, 1 kHz and 10 kHz are not presented here), whereas in the high-temperature region, $\chi(T)$ depends slightly on the magnetic field. This results in different Curie-Weiss temperatures θ_{CW} and almost the same effective magnetic moment; e.g., for $Ce_3Rh_4Sn_{13}$ (sample #2), $\theta_{CW} = 6$ K when χ is measured in magnetic field $B = 500$ Gs, while $\Theta_{CW} = 11.7$ K for data measured in $B = 10^4$ Gs. This effect could be attributed to spin fluctuations observed recently for both samples. The significant change in $1/\chi$ at ~ 160 K for $Ce_3Co_4Sn_{13}$ (indicated by an arrow in Fig. 1) could be of magnetic origin or result from a change of the crystallographic structure. To eliminate the possibility of a structural change at this temperature, we measured the x-ray diffraction patterns above and below this temperature, which show no change in the crystal structure (Fig. 2). The first inset of Fig. 2 shows the temperature dependence of the distance $d(T)$ between (532) crystallographic planes, obtained from the Bragg equation $\lambda = 2d \sin\theta(T)$ for diffraction line (532). The behavior of $d(T)$ is characteristic of typical thermal expansion behavior. A detailed analysis of the shape of this diffraction line with components $K_{\alpha 1}$ and $K_{\alpha 2}$ was conducted by fitting with the Gaussian function $f(\theta) = a + b/exp[(\theta - \theta_1)/\Delta_1]^2 + f/exp[(\theta - \theta_2)/\Delta_2]^2$, where θ_1 and θ_2 represent the Bragg reflection's maxima. It showed that the parameter Δ_2, which is proportional to the half-width of the $K_{\alpha 2}$ diffraction line, is temperature dependent (details in the second inset of Fig. 2), while Δ_1 is almost constant. Namely, Δ_2 increases in the T-range: ~ 150 K - 60 K upon cooling, and below 60 K it again reaches the value obtained above 130 K. One possible scenario is that there is a change of symmetry below $150 - 160$ K, probably due to some distinct distortion; e.g., of $Co(Sn2)_6$ trigonal prisms and/or $Sn1(Sn2)_{12}$ cages.[21] To confirm our hypothesis, we measured the (320) diffraction line vs. temperature. The intensity of this line reflects the largest diffraction effect on the Sn2 atoms, which leads to the maximum intensity in the x-ray diffraction pattern. In Fig. 2 (the lower right panel), the intensity of the (320) Bragg reflection exhibits a significant change at about 160 K, that can be explained by the local distortion of $Co(Sn2)_6$ prisms. The atomic positions and structural information, which was obtained from the full x-ray diffraction patterns presented in Fig. 2, are summarized for $Ce_3Co_4Sn_{13}$ in Table 1. The structures at $T = 300$ K, 120 K and 12 K were solved by Rietveld analysis and refined using the FULPROF package. By comparing the interatomic distances Sn1-Sn2, Ce-Sn2, and Co-Sn2 in $Ce_3Co_4Sn_{13}$, we observe that the distances $Sn1(Sn2)_{12}$, $Ce(Sn2)_4$, and $Ce(Sn2)_8$ are evidently temperature dependent, which suggests that the structure becomes locally distorted at $T = 120$ K and 12 K with respect to the structure at room temperature. In Fig. 3 we compare the structure of $Ce_3Co_4Sn_{13}$ highlighting the arrangement of the $Sn1(Sn2)_{12}$ isacohedras obtained at 293 K and 120 K, respectively with the values of the lattice parameters normalized to a at room temperature. The Sn atoms are yellow at $T = 293$ K, while the blue atoms exhibit the atomic positions of Sn at $T = 120$ K. The figure shows evidently a small local distortion of the $Sn1(Sn2)_{12}$ isacohedras and the $Co(Sn2)_6$ trigonal prisms. As was

previously shown,[11,25] there is high charge density between Co (or Rh) and Sn2 atoms, which implies strong covalent bonding interactions. A small change of a local symmetry can modify the electronic structure near the Fermi level, which drives different magnetic and electric transport properties as a consequence.

The magnetic susceptibility can be described by a modified Curie-Weiss law $\chi = \chi_0 + C/(T - \theta_{CW})$, where χ_0 is the temperature-independent part of the magnetic susceptibility, C is a Curie constant, and Curie-Weiss temperature θ_{CW} is -1.78, -1.2, and -2.3 K for samples (♯1), (♯2), and $Ce_3Co_4Sn_{13}$, respectively. The fit also gives an effective magnetic moment of 2.4, 2.6 and 2.7 μ_B, respectively. These values are all close to the theoretical value of 2.54 μ_B/Ce expected for a free Ce^{3+} ion, indicating that the magnetic moments of Ce ions are well localized. The inset to Fig. 1 shows the low-temperature $\chi \sim T^{-n}$ behavior with $n = 0.67$, 0.70, and 0.64, for samples (#1), (#2), and $Ce_3Co_4Sn_{13}$, respectively. Magnetic order has not been explicitly observed in $\chi(T)$ data, however, power-law behavior in $\chi(T)$ and a logarithmic C/T behavior in less than half of a decade (as will be discussed) at low temperatures could be related to the proximity of a magnetic QCP.[3]

The magnetization M vs. magnetic field isotherms for $Ce_3Rh_4Sn_{13}$ (#2) are shown in Fig. 4. They are well approximated by the Langevin function $L(y) = \coth(y) - 1/y$, where $y = \mu B/k_BT$ with total magnetic moment $\mu = 0.54$ μ_B (obtained for the isotherm measured at $T = 1.9$ K). Similar $M(B)$ isotherms are measured for samples (#1) and $Ce_3Co_4Sn_{13}$, which are also well described by the Langevin function with a magnetic moment of 0.48 μ_B. The magnetization does not show any hysteresis in the field dependence of magnetization M and is not an universal function of B/T, which rules out[26] superparamagnetic behavior.

In Fig. 5, we present the magnetization M vs. B isotherms for $La_3Rh_4Sn_{13}$. The data are interesting because a strong diamagnetic component is observed in the magnetic susceptibility, and a symmetric hysteresis loop at $T = 1.9$ K is characteristic of irreversible superconductivity. A very similar $M(B)$ behavior was obtained for $La_3Co_4Sn_{13}$. $La_3Rh_4Sn_{13}$ superconducts below a critical temperature $T_c = 2.6$ K. Moreover, the magnetic susceptibility, measured between T_c and 300 K in a magnetic field of 0.1 T, obeys a T^2-dependence very well, indicating the presence of ferromagnetic spin-fluctuations (as presented in panel (b)). A spin fluctuation characteristic temperature $T_{SF} \sim 1090$ K is estimated by analyzing the data with the spin-fluctuation model[27] $\chi \sim 1 - (T/T_{SF})^2$. It would seem that the superconductivity in $La_3Rh_4Sn_{13}$ and in $La_3Co_4Sn_{13}$ can be mediated by magnetic fluctuations, as has been reported for $Ca_3Ir_4Sn_{13}$ (Ref. 14). It is commonly believed, that Cooper pairs are formed *magnetically* in some Ce-based heavy fermions with *unconventional* superconductivity; e.g., in $CeRh_2Si_2$,[28] $CePd_2Si_2$,[13], or $CeRhIn_5$.[29] In the case of $La_3Rh_4Sn_{13}$ this suggestion seems to be too far-fetched speculation. On the contrary, it was shown[11,25] that the calculated high DOS at the Fermi level strengthens the spin fluctuations in $La_3M_4Sn_{13}$, which than suppress superconductivity. It is of interest to get an insight into the possible origin of the spin fluctuations in $La_3Rh_4Sn_{13}$. Former calculations with LSDA+U approximation[11] results in almost zero magnetic spin moments on Rh and Sn, however, since there is a significant contribution of Rh states to the Fermi surface, the *nesting* instabilities might be the origin for the observed spin fluctuations. A very similar nesting instabilities which generate the spin fluctuation effects of Rh 4d electrons were suggested for $CeRhSn_2$[31] and $CeRh_2Sn_4$.[30]

B. Specific heat

Figs. 6-8 compare the low-temperature specific heat of $Ce_3Rh_4Sn_{13}$ and $Ce_3Co_4Sn_{13}$. Both $C(T)$ and $C(T)/T$ exhibit a broad maximum situated at ~ 0.7 K with maximum value of $C/T = 4.3$ J/mole-Ce-K^2. By applying a magnetic field, the peak is suppressed in absolute value and shifts to higher temperatures. A very similar result was obtained previously for both compounds.[3,5] The low temperature heat capacity gives magnetic entropy $S_{magn} = R \ln 2$ at about 2 K (in Fig. 9) indicating that the peak in C/T represents the behavior of the ground state doublet, as was previously confirmed by inelastic neutron scattering studies,[9] and a weak Kondo effect. The splitting of the ground state doublet was attributed to the presence of an internal field (i.e., Zeeman splitting) in the presence of short range magnetic order. Small Kondo temperatures T_K of about 1.6 K for $Ce_3Rh_4Sn_{13}$ and $T_K = 1.2$ K for $Ce_3Co_4Sn_{13}$ samples were obtained independently from magnetoresistivity,[5] specific heat data at magnetic field approximated by the $S = 1/2$ Kondo impurity models,[3,5] inelastic neutron scattering,[9,19] and neutron diffraction studies.[8]

The Kondo singlet ground state has a universal linear specific heat given by $C_{el} = \gamma T/T_K$ at the lowest temperatures. An enhancement of the electronic specific heat coefficient $\gamma = Rln2/T_K$ is expected of ~ 3.8 J/mol-K^2-Ce for the both $Ce_3Rh_4Sn_{13}$ and $Ce_3Co_4Sn_{13}$ compounds, if $T_K \cong 1.5$ K, while the measured γs are much larger. Inside this simple estimate, the low-T broad maximum in the specific heat data signals the additional contribution of short-range-like magnetic order to the entropy. In zero magnetic field a satisfactory fit to the specific heat data was recently achieved assuming half of the entropy is due to single impurity effects and half is due to a Schottky-like contribution.[3,32] We note that magnetic order or short-range magnetic order has been obtained from our recent computational studies[11] for the stoichiometric $Ce_3Rh_4Sn_{13}$ compound. Within the VCA approach, the calculated total energy of $Ce_3Rh_4Sn_{13}$ versus magnetic moment shows a weak and broad minimum at about 1.8 μ_B/cell, while

the inclusion of small concentrations of Sn 2a vacancies removes the energy minimum for $Ce_3Rh_4Sn_{12.95}$ due to its magnetic ground state.[33] This indicates that the system is magnetically unstable. The reduced magnetic moment of $Ce_3M_4Sn_{13}$ and magnetic correlations indicated by experiments could be explained either by the many-body Kondo screening effect or strong spin fluctuations. Comparative study of the specific heat for $Ce_3Rh_4Sn_{13}$ and $Ce_3Co_4Sn_{13}$ suggests a similar mechanism is responsible for the low-temperature thermodynamic properties of both systems. The small maximum at 0.7 K in $C(T)$ data of the off stoichiometry sample (sample #1) and the kink in $C(T)/T$ (in Fig. 7) could be attributed to a magnetic phase transition generated by vacancies at the 2a Sn sites. The electrical resistivity also shows a maximum at this temperature (see below).

C. Electronic structure and Anderson width Δ obtained from the core-level 3d XPS spectra

The HF state is modeled microscopically by the periodic Anderson model. For the Kondo lattice state, the ground state of a Ce-based compound is very sensitive to both the magnitude of the hybridization energy $V_{cf} \sim [\Delta/N(\epsilon_F)]^{1/2}$ between f and conduction electron states and the concentration of carriers, n_e, as is rationalized within the framework of the periodic Anderson model.[34] The microscopic parameters of the Anderson-lattice model: V_{cf} and the occupancy of the f shell, n_f, can be determined experimentally from the Ce 3d x-ray photoemission spectra using the Gunnarsson-Schönhammer (GS) theory[35], which is based on the Anderson-impurity model.[36] In Fig. 10, we plot the Ce 3d core-level XPS spectra for $Ce_3Rh_4Sn_{13}$[37] and $Ce_3Co_4Sn_{13}$. For comparison, we also present the La 3d core-level XPS spectra obtained for the reference compounds, respectively. Each spin-orbit (SO) set of the Ce or La 3d XPS lines consists of two contributions labeled as f^n and f^{n+1}, where $n = 0$ or $n = 1$ for La and Ce, respectively. The main components of the $3df^n$ lines appear when the core hole is screened by conduction electrons, while the $3df^{n+1}$ satellites, located on the low-energy side of the main peaks, result from a $4f^n \rightarrow 4f^{n+1}$ transition during the photoemission process. In consequence, the core hole is screened by an extra $4f$ electron in an excitation-like level centered on the core-ionized atom. The probability of transferring an electron to this screening level depends on its coupling to the other occupied states. Consequently, the f^{n+1} contributions in the measured Ce or La 3d XPS spectra reflect the degree of hybrydization between the $4f$ and conduction band states in the initial state.[38] The separation of the overlapping peaks in the 3d XPS spectra was carried out on the basis of the Doniach-Šunjić interpretation scheme.[39] For Ce, the main components, $3d^9_{5/2}4f^1$ and $3d^9_{3/2}4f^1$, exhibit a spin-orbit splitting of magnitude $\Delta_{SO} = 18.6$ eV. The presence of the $3d^94f^2$ components reflects the intra-atomic hybridization between the $4f$-electrons and conduction band. From the analysis of these spectra (for details on the procedure see also Ref. 40), one obtains the hybridization energy Δ, with accuracy on the order of 20%. Some error in the determination of Δ is due to the uncertainty in the intensity ratio $3d^9f^1 : 3d^9f^2$, which is directly related to the accuracy of the decomposition of the spectrum, as well as to proper background subtraction. Such an estimate yields $\Delta \sim 50$ meV for $Ce_3Rh_4Sn_{13}$ samples, while $\Delta \approx 130$ meV for $Ce_3Co_4Sn_{13}$ suggests a stronger hybridization effect. In case of $La_3Rh_4Sn_{13}$ and $La_3Co_4Sn_{13}$, the parameter $\Delta \sim 70$ meV can be obtained on the base of GS theoretical model from the intensity ratio $I(f^1)/[I(f^0) + I(f^1)]$. The relatively high value of Δ for La is consistent with the general finding that hybridization tends to be smaller in Ce compounds than in their La counterparts due to the larger contraction of the $4f$ orbitals in Ce. We also conclude that the energy Δ is larger for $Ce_3Co_4Sn_{13}$ than for the Rh sample as a consequence of stronger f-conduction electron hybridization, defined by the hybridization energy V_{cf} (see below the discussion of the valence band XPS spectra). Another reason is the larger DOS at the Fermi level, $N(\epsilon_F)$, in $Ce_3Co_4Sn_{13}$. Indeed, the calculated DOS at ϵ_F for $U = 6$ eV is about twice as large for $Ce_3Co_4Sn_{13}$[25] than for $Ce_3Rh_4Sn_{13}$.[11]

We did not observe any additional peaks in the Ce 3d XPS spectra at a distance of ∼ 11 eV from the main photoemission lines, which could be assigned to the Ce $3d^94f^0$ final state, giving evidence for the stable configuration of Ce^{3+}. Additional evidence for Ce^{3+} ions in $Ce_3M_4Sn_{13}$ is shown in Fig. 11. The Ce 4d XPS spectra do not show additional peaks at a binding energies of $\sim 118-124$ eV, which could be attributed to $4f^94f^0$ final states (for details, see Refs. 41,42).

Fig. 12 displays the valence band (VB) XPS spectra for $Ce_3M_4Sn_{13}$ and $La_3M_4Sn_{13}$. In the VB XPS spectra of the Co-samples, the most intense peak is located at about 1.5 eV, which originates mainly from the Co 3d states hybridized with 5p states from Sn (c.f. Ref. 25). In the case of the Rh-samples, the maximum in the total DOS is more deeply located in the electronic band (about 3 eV) and originates mainly from the Rh 4d states, hybridized with Sn 5p states.[11] It is clearly visible in Fig. 12 that the Ce $4f$ states give a small contribution to the measured spectra. Moreover, the band structure calculations in the LSDA+U approximation show that the DOS in the vicinity of the Fermi level is nearly the same for $Ce_3M_4Sn_{13}$ and the reference $La_3M_4Sn_{13}$ compounds.[11,25] This finding also lends support to the picture that the Ce $4f$ states are almost localized and the RKKY magnetic interactions among the localized $4f$ moments determine the possible magnetic ground state properties of both $Ce_3M_4Sn_{13}$, where M = Rh or Co. However, the VB XPS spectra suggest that the hybridization between the f and conduction electron states is stronger in the case of $Ce_3Co_4Sn_{13}$. This could also be a reason for the different resistivity $\rho(T)$ behavior

in Co-based $Ce_3M_4Sn_{13}$ samples (as will be discussed). From the *ab initio* calculations, the flat $4f$ bands in the energetic dispersion curves $E(k)$ near ϵ_F and the relatively high DOS are both indicative of a large electron effective mass and a small electron mobility, which is smaller in $Ce_3Co_4Sn_{13}$ than in $Ce_3Rh_4Sn_{13}$. In addition, the calculations show a pseudogap along the $\Gamma - R$ and $\Gamma - X$ directions, which indicates a semimetal character for both $Ce_3M_4Sn_{13}$ compounds (M = Rh, Co) implied by the entropy and electrical resistivity measurements.

D. Electrical resistivity under magnetic field and pressure

Electrical resistivity data for $Ce_3M_4Sn_{13}$ are shown in Figs. 13 - 16. In the inset to Fig. 14, we also show the resistivity of the reference compounds $La_3Rh_4Sn_{13}$ and $La_3Co_4Sn_{13}$ with a sudden drop to zero at $T_c = 3.8$ K and 2.9 K, respectively, due to their superconducting transition. These temperatures are consistent with the magnetic susceptibility data. For $Ce_3M_4Sn_{13}$ and $La_3M_4Sn_{13}$ (M = Rh, Co) compounds, the absolute magnitude of the resistivity at room temperature is relatively high because of several reasons in the scattering processes of electrons: the involvement of strong correlation effect in case of Ce-based compounds, atomic defects, as well as grain boundaries and other defects of metallurgical nature. The $\rho(T)$ data cannot be approximated by the Bloch-Grüneisen-Mott formula:

$$\rho(T) = \rho_0 + \rho_{ph} + \rho_M, \tag{1}$$

where

$$\rho_{ph} = 4RT\left(\frac{T}{\Theta_D}\right)^4 \int_0^{\frac{\Theta_D}{T}} \frac{x^5 dx}{(e^x - 1)(1 - e^{-x})}, \tag{2}$$

$$\rho_M = -KT^3, \tag{3}$$

and ρ_0 is the residual resistivity. Θ_D is the Debye temperature, R is the gas constant, and the cubic term KT^3 describes interband scattering processes.[43] From the analysis of the $\rho(T)$ data, it is clear that these materials exhibit metallic conductivity with a spin-fluctuation contribution coming from the $4d/3d$ electrons and crystal field effects in the case of $Ce_3M_4Sn_{13}$.

First, we discuss the $\rho(T)$ behavior of the La-based compounds in the metallic state ($T_c < T < T_{coh}$, where T_{coh} determines the quantum coherence effects in Ce-based compounds). Below 20 K for $La_3Rh_4Sn_{13}$ and 15 K for $La_3Co_4Sn_{13}$, the resistivity is well fitted by an expression $\rho \sim AT^2$ with $A = 0.03$ $\mu\Omega$cm/K^2 and 0.09 $\mu\Omega$cm/K^2, respectively. For materials with non-magnetic ground states, this behavior is expected to be that of a Fermi liquid.[44] The obtained value for A is consistent with other nonmagnetic HF systems, e.g., for $CeSn_3$ $A = 0.001$ $\mu\Omega$cm/K^2,[45] for $CePd_3$ $A = 0.1$ $\mu\Omega$cm/K^2,[46] and for $CeAl_3$ $A = 35$ $\mu\Omega$cm/K^2.[47] The $\rho \sim T^2$ behavior is also predicted within the paramagnon model[48] for magnetic HF systems. The resistivity of $Ce_3M_4Sn_{13}$, when $\rho(T)$ is subtracted by the phonon contribution does not show $\Delta\rho \sim T^2$ behavior. Resistivity exhibits, however, the coherence effect in Fig. 14*b* with $\Delta\rho \sim -lnT$ behavior above ~ 30 K. Using the standard expression for the virtual bound state width,[36] we obtained that $T_{coh} \sim k_B^{-1}\pi V_{cf}^2 N(\epsilon_F) \approx \Delta/k_B \cong 200$ K, with the correct order of magnitude. On the basis of these results, we have singled out both the spin-fluctuation contribution coming from the d electrons of element M and the Kondo-type scattering above coherence of the f states.

In Fig. 14, the temperature dependence of the resistivity for $Ce_3Co_4Sn_{13}$ is quite different. It displays a metallic behavior above ~ 160 K, while below this temperature, the $\rho(T)$ behavior is similar to that of $Ce_3Rh_4Sn_{13}$ and the La-reference compounds. Since x-ray diffraction analysis has suggested a possible local distortion below ~ 160 K (see Fig. 2), this intriguing $\rho(T)$ dependence might be accompanied by a change of the electronic structure. Earlier, we argued that even a small change of the local symmetry of the trigonal Sn2 prisms around Rh can significantly change the energy dispersion near the Fermi level. From *ab initio* calculation results, a pseudogap along the high symmetry **k**-vector directions and a semimetallic character of both $Ce_3Rh_4Sn_{13}$ and $Ce_3Co_4Sn_{13}$ compounds are predicted. Moreover, this three-dimensional network of corner-sharing Co/Rh(Sn2)$_6$ prisms generates two different cages occupied by Ce and Sn1 atoms; a small change of the local symmetry (e.g., of the Co/Rh(Sn2)$_6$ prisms) leads to variation in the charge density of the surrounding Ce ions. As a result, we expect stronger hybridization effects in *distorted* $Ce_3Co_4Sn_{13}$ than in $Ce_3Rh_4Sn_{13}$, as was experimentally confirmed by XPS. This scenario explains the observed transition at ~ 160 K between the semimetallic and metallic behavior in $Ce_3Co_4Sn_{13}$. For this compound, the hybridization parameter Δ is twice as large as it is in $Ce_3Rh_4Sn_{13}$. Furthermore, the electrical resistivity of $Ce_3Co_4Sn_{13}$ under pressure fully supports this interpretation. In Fig. 16, the pressure effect is small in the metallic state, i.e., above ~ 160 K, while for $T \lesssim 160$ K, the resistivity increases with pressure. The pressure effect on the electrical resistivity of heavy-fermion

systems can be understood by broadening the hybridization effect and reducing the energy difference between the Fermi level and $4f$ levels (c.f. Refs. 49,50). Fig. 15 displays the pressure-increased resistivity of $Ce_3Rh_4Sn_{13}$ in the whole T-range, which does not suggest any structural change in this compound. Moreover, a clear coherence effect with $\Delta\rho \sim -\ln T$ behavior is observed. The logarithmic decrease at high temperature is preserved under pressure and with no variation of the slope $\partial\Delta\rho/\partial \ln T$ (c.f., Ref. 49).

Finally, we discuss the electrical resistivity under external pressure at low temperature. Figs. 15 and 16 exhibit a logarithmic increase of $\rho(T)$ between $\sim$ 3 K and $\sim$ 10 K due to the singlet Kondo impurity effect. We can also approximate the low-T resistivity by an activated law: $\rho \sim \exp(\Delta E/k_BT)$, with fitting parameters $\Delta E = 0.14$ K for $Ce_3Rh_4Sn_{13}$ and 0.32 K for $Ce_3Co_4Sn_{13}$, respectively, in the T-range 4.5 K to $\sim$ 15 K. However, the energy gaps ΔE are two orders in magnitude smaller that the calculated pseudogap for these materials; therefore the $-\ln T$ behavior is much more probable than the activated one. The maximum in $\rho(T)$ at about 2 K is generally due to the magnetic correlations; however, the physics of the ground state of both $Ce_3M_4Sn_{13}$ systems is more complicated. The nature of this low-T maximum reflects an interplay of crystal-field effects, magnetic correlations, and the characteristics of heavy-Fermion metals.

IV. CONCLUSIONS

The principal purpose of this work was to determine the role of on-site hybridization between the $4f$-electron and conduction electron states in the physical properties of $Ce_3Rh_4Sn_{13}$ and $Ce_3Co_4Sn_{13}$. We have presented a comparative analysis of the magnetic and electric transport properties of both systems.

The reference compounds, $La_3M_4Sn_{13}$, exhibit spin fluctuations and superconductivity. Spin fluctuations are also observed in $Ce_3M_4Sn_{13}$ in the resistivity $\rho \sim T^2$ data. Our thermodynamic investigations confirmed that the compounds $Ce_3M_4Sn_{13}$ (M = Rh, Co) are strongly correlated f-electron materials. The comparative studies show, however, a significant difference between the Co and Rh-based samples. $Ce_3Co_4Sn_{13}$ has more strongly hybridized f and conduction electrons than does $Ce_3Rh_4Sn_{13}$. The stronger hybridization energy Δ and the small structural distortion leads to the semimetal-metal transition at about 160 K that is not characteristic of $Ce_3Rh_4Sn_{13}$. We also note that the electronic structure determines the electric transport properties of both materials. The relatively high electrical resistivity in the paramagnetic region results from the semimetallic character of both samples. The structural distortion in $Ce_3Co_4Sn_{13}$ can, however, modify the energy dispersion dependencies $E(\mathbf{k})$ in the high symmetry directions in the Brillouin zone. As a consequence, there is a possible metallic phase above $\sim$ 160 K.

V. ACKNOWLEDGMENTS

One of us (A.Ś.) is grateful for the hospitality at the University of California, San Diego (UCSD). He also thanks the Polish Ministry of Science and Higher Education for financial support from project No. N N202 032137. One of us (M.F.) thanks the National Science Centre (NCN) for financial support, on the basis of decision No. DEC-2011/01/N/ST3/03476. Research at UCSD was supported by the U.S. Department of Energy under Grant No. DE-FG02-04ER46105. We thank the National Science Centre (NCN) for financial support on the basis of decision No. DEC-2011/01/N/ST3/03476.

[1] J. P. Remeika, G.P. Espinosa, A. S. Cooper, H. Barz, J.M. Rowel, D. B. McWhan, J. M. Vandenberg, D. E. Moncton, Z. Fizk, L. D. Woolf, H. C. Hamaker, M. B. Maple, G. Shirane, and W. Thomlinson, Sol. State Commun. **34**, 923 (1980); J. L. Hodeau, M. Marezio, J. P. Remeika, and C. H. Chen, *ibid.* **42**, 97 (1982).

[2] C. Israel, E.M. Bittar, O. E. Agüero, R. R. Urbano, C. Rettori, I. Torriani, P. G. Pagliuso, N. O. Moreno, J. D. Thompson, M. F. Hundley, J. L. Sarrao, and H. A. Borges, Physica B **359-361**, 251 (2005).

[3] A. L. Cornelius, A. D. Christianson, J. L. Lawrence, V. Fritsch, E. D. Bauer, J. L. Sarrao, J. D. Thompson, and P. G. Pagliuso, *ibid.* **378-380**, 113 (2006).

[4] E. L. Thomas, H. -O. Lee, A. N. Bonkston, S. MaQuilon, P. Klavins, M. Moldovan, D. P. Young, Z. Fisk, and J. Y. Chan, J. Sol. State Chem. **179**, 1642 (2006).

[5] U. Köhler, A. Pikul, N. Oeschler, T. Westerkamp, A. M. Strydom, and F. Steglich, J. Phys.:Condens. Matter **19**, 386207 (2007).

[6] H. Sato, T. Fukuhara, S. Iwakawa, Y. Aoki, I. Sakamoto, S. Takayanagi, and N. Wada, Physica B **186-188**, 630 (1993).

[7] D. Niepmann, R. Pöttgen, K. M. Poduska, F. J. DiSalvo, H. Trill, and B. D. Mosel, Z. Naturf. B **56**, 1 (2001).

[8] A. D. Christianson, E. A. Goremychkin, J. S. Gardner, H. J. Kang, J. -H. Chung, P. Manuel, J. D. Thompson, J. L. Sarrao, and J. M. Lawrence, Physica B **403**, 909 (2008).

[9] D. T. Adroja, A. M. Strydom, A. P. Murani, W. A. Kockelmann, and A. Fraile, Physica B **403**, 898 (2008).

[10] Y. Ōduchi, C. Tonohiro, A. Thamizhavel, H. Nakashima, S. Morimoto, T. D. Matsuda, Y. Haga, K. Sugiyama, T. Takeuchi, R. Settai, H. Hagiwara, and Y. Ōnuki, J. Magn. Magn. Mater. **310**, 249 (2007).

[11] M. Gamża, W. Schnelle, A. Ślebarski, U. Burkhardt, R. Gumeniuk, and H. Rosner, J. Phys.:Condens. Matter **20**, 395208 (2008).

[12] In some heavy fermions the superconductivity occurs in the vicinity of the quantum critical point. For example, the superconductivity appears in the vicinity of antiferromagnetic QCP under the critical pressure in $CePd_2Si_2$ and $CeIn_3$.[13] Very recently,[14] the coexistence of superconductivity and ferromagnetic spin fluctuations were discovered in the isostructural compound $Ce_3Ir_4Sn_{13}$, and this material is expected to be on the border of ferromagnetism. For the system $(Ca_xSr_{1-x})_3Ir_4Sn_{13}$ the superlattice transition temperature $T^\star$ can be suppressed to $T = 0$ by both chemical and physical pressure, enabling the first comprehensive investigation of a superlattice QCP and its interplay with superconductivity in a three-dimensional charge density wave system.[15]

[13] N. D. Mathur, F. M. Grosche, S. R. Julian, I. R. Walker, D. M. Freye, R. K. W. Haselwimmer, and G. G. Lonzarich, Nature (London) **394**, 39 (1998).

[14] J. Yang, B. Chen, Ch. Michioka, and K. Yoshimura, J. Phys. Soc. Jpn. **79**, 113705 (2010).

[15] L. E. Klintberg, S. K. Goh, P. L. Alireza, P. J. Saines, D. A. Tompsett, P. W. Logg, J. Yang, B. Chen, K. Yoshimura, and F.M. Grosche, arXiv:1202.3282v1 [cond-mat.str-el] 15 Feb 2012

[16] T. F. Smith, C. W. Chu, and M. B. Maple, Cryogenics **9**, 54 (1969).

[17] Y. Baer, G. Busch and P. Cohn, *Rev. Sci. Instrum.* **46**, 466 (1975).

[18] C. Nagoshi, H. Sugawara, Y. Aoki, S. Sakai, M. Kohgi, H. Sato, T. Onimaru, and T. Sakakibara, Physica B **359-361**, 248 (2005).

[19] A. D. Christianson, J. S. Gardner, H. J. Kang, J. -H. Chung, S. Bobev J. L. Sarrao, and J. M. Lawrence, J. Magn. Magn. Mater. **310**, 266 (2007).

[20] In the all references known, $Ce_3Co_4Sn_{13}$ is reported as a *nonmagnetic* compound with the short-range magnetic order indicated by the low-temperature specific heat data.

[21] Room temperature single crystal x-ray diffraction on some compounds of this family; e.g., $La_3Rh_4Sn_{13}$ (Ref. 22), $Gd_3Ir_4Sn_{13}$ (Ref. 23), or $Sr_3Ir_4Sn_{13}$ (Ref. 15) confirmed the I-phase structure ($Pm\bar{3}n$) which in case of $(Sr/Ce)_3Ir_4Sn_{13}$ shows a transition to the superlattice variant $I\bar{4}3d$ as a result of deformation of the $Sn1(Sn2)_{12}$ cages.

[22] P. Bordet, D.E. Cox, G.P. Espinoza, J.L. Hodeau, and M. Marezio, Solid State Commun. **78**, 359 (1991).

[23] C. Nagoshi, R. Yamamoto, K. Kuwahara, H. Sagayama, D. Kawana, M. Kohgi, H. Sugawara, Y. Aoki, H. Sato, T. Yokoo, and M. Arai, J. Phys. Soc. Jpn., **75**, 044710 (2006).

[24] K. Momma and F. Izumi, J. Appl. Crystallogr., **44**, 1271 (2011).

[25] G. Zhong, X. Lei, and J. Mao, Phys. Rev. B **79**, 094424 (2009).

[26] C. M. Hurd, Contemp. Phys. **23**, 469 (1982).

[27] R. J. Trajnor, M. B. Brodsky, and H. V. Culbert, Phys. Rev. Lett. **34**, 1019 (1975).

[28] R. Movshovich, T. Graf, D. Mandrus, J.D. Thompson, J.L. Smith, and Z. Fisk, Phys. Rev. B **53**, 8241 (1996).

[29] T. Park, V.A. Sidirov, F. Ronning, J.-X. Zhu, Y. Tokiwa, H. Lee, E.D. Bauer, R. Movshovich, J. Sarrao, and J.D. Thompson, Nature **456**, 366 (2008).

[30] M. Gamża, W. Schnelle, R. Gumeniuk, Yu. Prots, A. Ślebarski, H. Rosner, and Yu. Grin, J. Phys.:Condens. Matter **21**, 325601 (2009).

[31] M. Gamza, A. Ślebarski, and H. Rosner, J. Phys.:Condens. Matter **20**, 025201 (2008).

[32] B. E. Light, R. S. Kumar, A. L. Cornelius, P. G. Pagliuso, and J. L. Sarrao, Phys. Rev. B **69** , 024419 (2004).

[33] For the larger simulated concentrations of vacancies the energy minimum corresponding to the magnetic ground state is evidently calculated again.[11]

[34] R. Doradziński and J. Spałek, Phys. Rev. B **56**, 14239 (1977); Phys. Rev. B **58**, 3293 (1998).

[35] O. Gunnarsson and K. Schönhammer, Phys. Rev. B **28**, 4315 (1983); J. C. Fuggle, F. U. Hillebrecht, Z. Zolnierek, R. Lässer, Ch. Freiburg, O. Gunnarsson, and K. Schönhammer, Phys. Rev. B, **27**, 7330 (1983).
[36] P. W. Anderson, Phys. Rev. **124**, 41 (1961).
[37] The Ce 3*d* core-level XPS spectra are within an experimental error the same for the $Ce_3Rh_4Sn_{13}$ samples (♯1) and (♯2).
[38] J. C. Fuggle, M. Campagna, Z. Zolnierek, R. Lässer, and A. Platau, Phys. Rev. Lett. **45**, 1597 (1980).
[39] S. Doniach and M. Šunjić, J. Phys. C **3**, 286 (1970).
[40] A. Ślebarski, M. Radłowska, T. Zawada, M. B. Maple, A. Jezierski, and A. Zygmunt, Phys. Rev. B **70**, 235112 (2004); A. Ślebarski, T. Zawada, J. Spałek, and A. Jezierski, Phys. Rev. B **70**, 235112 (2004).
[41] Y. Baer, R. Hauger, Ch. Zürcher, M. Campagna, and G.W. Wertheim, Phys. Rev. B **18**, 4433 (1978).
[42] A. J. Signorelli and R. G. Hayes, Phys. Rev. B **27**, 7330 (1983).
[43] N. F. Mott and H. Jones *The Theory of the Properties of Metals and Alloys*, Oxford University Press, (1958), p. 240.
[44] C. M. Varma, *Valence Instabilities and Related Narrow Band Phenomena* ed. R.D. Parks (New York: Plenum, 1977.
[45] B. Staliński, Z. Kletowski, and Z. Henkie, Phys. Stat. Solidi A **19**, K165 (1973).
[46] P. Scoboria, J. E. Crow, and T. Mihalisin, J. Appl. Phys. **50**, 1895 (1979).
[47] K. Andres, J.E. Graebner, and H. Ott, Phys. Rev. Lett. **35**, 1779 (1975).
[48] O. R. Jullien, M. T. Beal-Monod, and B. Coqblin, Phys. Rev. B **9**,1441 (1974).
[49] A. Najib, J. Beille, R. Lahiouel, and J. Pierre, J. Phys. F:Met. Phys. **17**, 2395 (1987).
[50] H. D. Yang and W. H. Lee, Phys. Rev. B **43**, 3664 (1991).

Figures

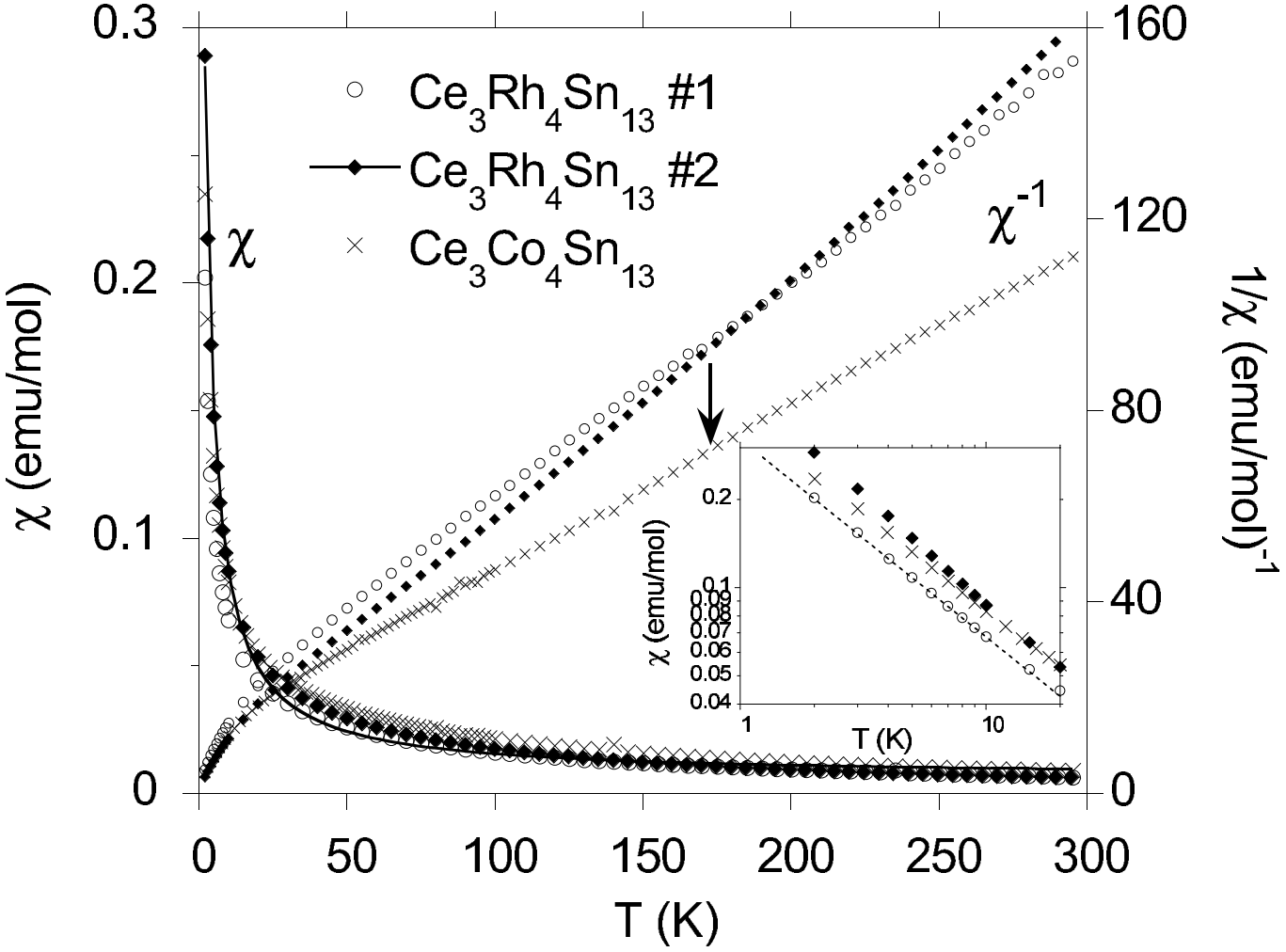

FIG. 1: DC magnetic susceptibility, χ, measured in a magnetic field of 500 Gs and $1/\chi$ vs. temperature for $Ce_3Rh_4Sn_{13}$ samples (#1 and #2) and for $Ce_3Co_4Sn_{13}$. The line represents the approximation of the $\chi(T)$ data by the modified Curie-Weiss law $\chi = \chi_0 + C/(T - \theta_{CW})$ between 2 K and 300 K; the fit is not enough good. The $\chi(T)$ data are well described by this expression in the temperature region $T > 15$ K. The inset displays the low-temperature $\chi(T)$ data in a log-log scale.

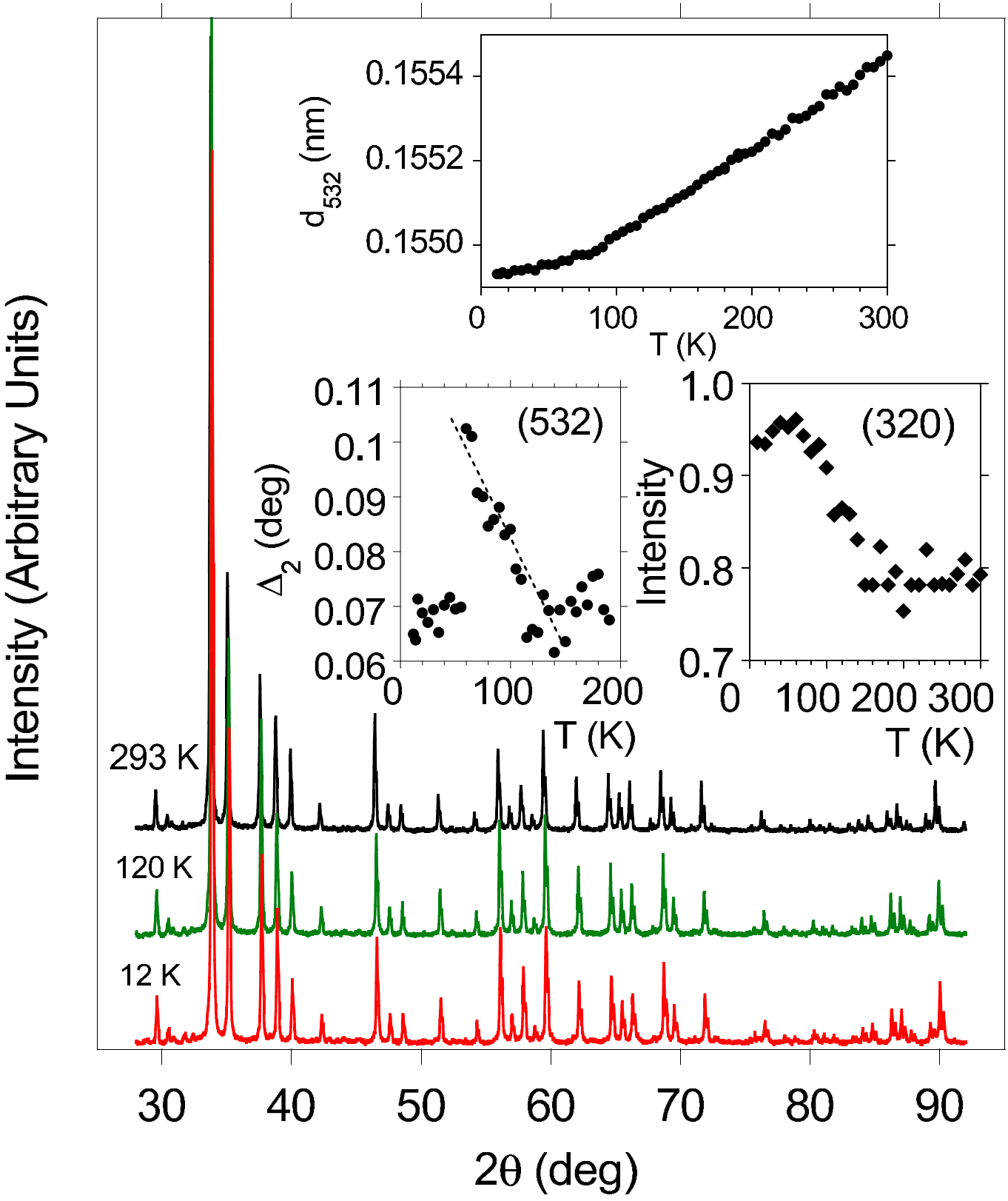

FIG. 2: X-ray diffraction (XRD) of $Ce_3Co_4Sn_{13}$ with Cu K_α radiation and at different temperatures. The upper inset displays the temperature change of the (532) XRD line between 12 K and 300 K. The lower panel displays the temperature dependence of the parameter Δ_2, which is proportional to the half-width of the $K_{\alpha 2}$ diffraction peak. The lower right panel shows the temperature dependence of the intensity of the (320) diffraction line

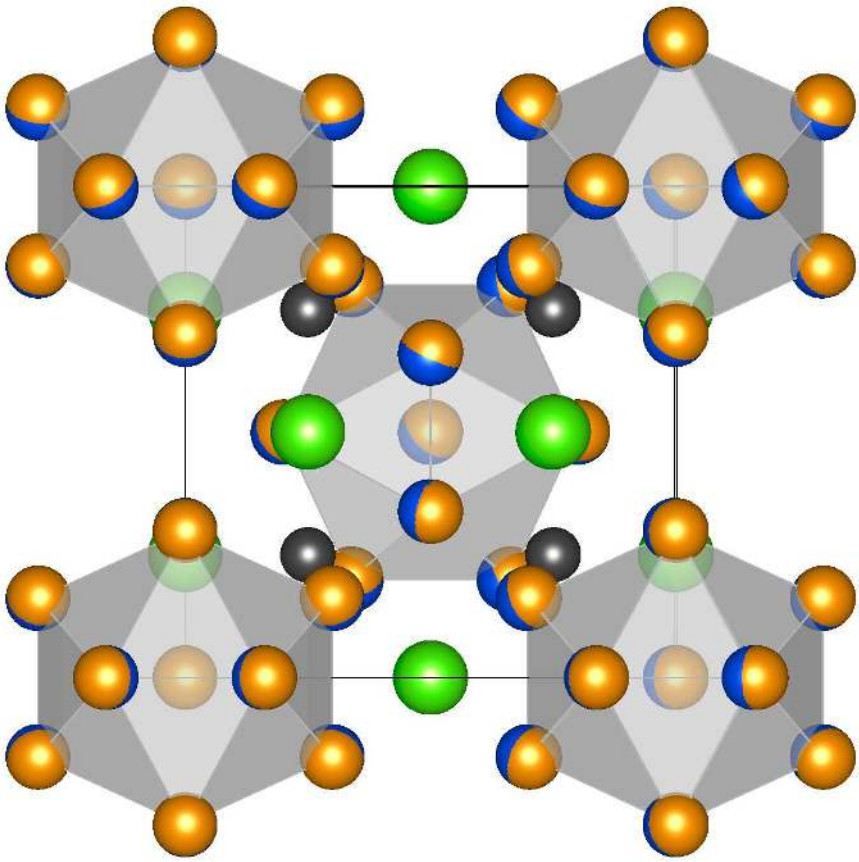

FIG. 3: The structure of $Ce_3Co_4Sn_{13}$ at the room temperature and at $T = 120$ K highlighting the arrangement of the $Sn1(Sn2)_{12}$ icosahedra, with Sn atoms at $T = 293$ K (yellow) and at $T = 120$ K (blue). Ce (green circles) and Co (black circles) are represented as isolated atoms. The lattice parameters measured at two different temperatures are normalised in the figure to a value obtained at $T = 293$ K. The drawing of the figure is produced by VESTA[24].

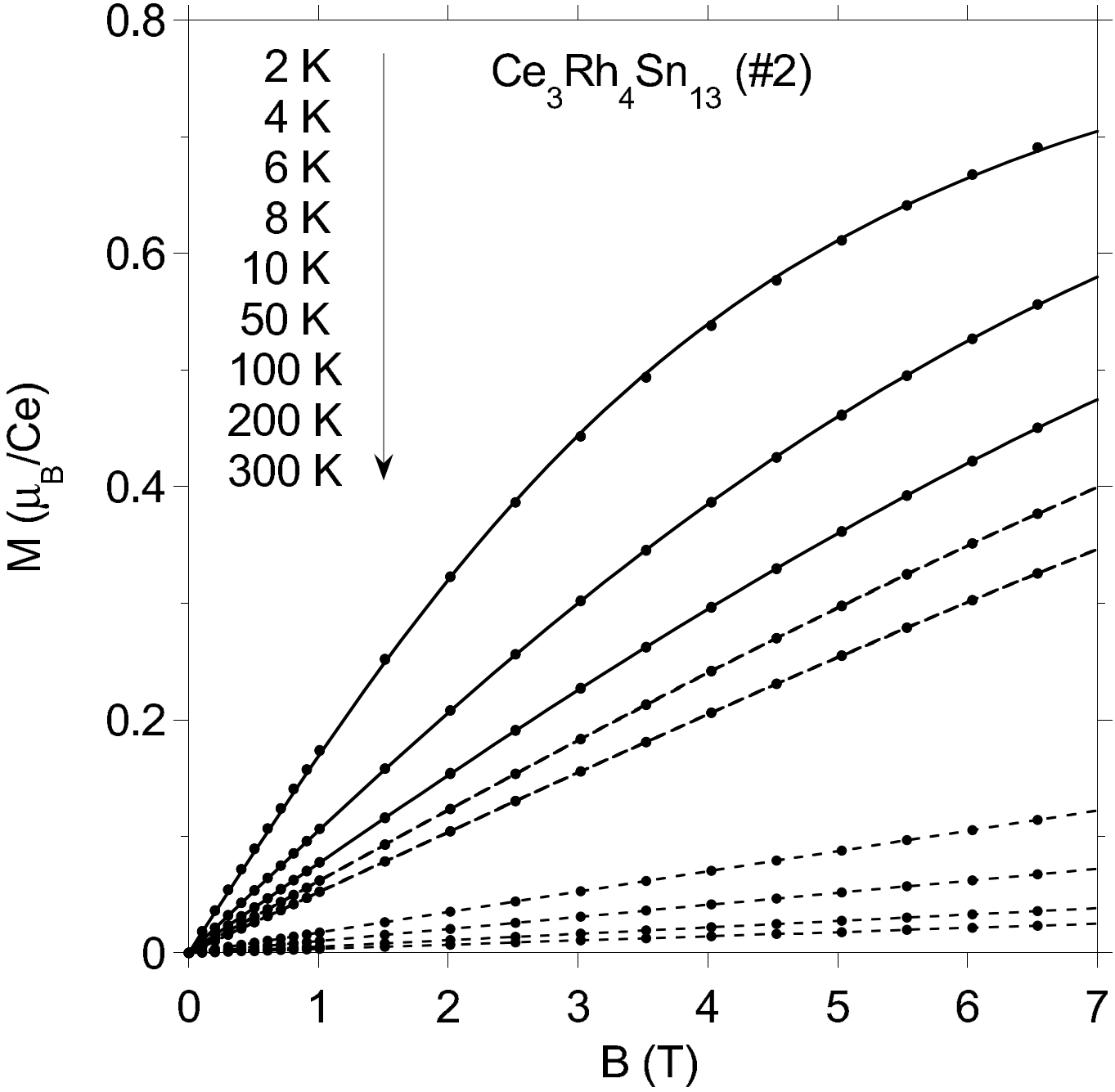

FIG. 4: Magnetization M vs. magnetic field B measured at different temperatures for $Ce_3Rh_4Sn_{13}$ (sample #2). The solid lines are fits of the Langevin function to the magnetization data at $T = 2, 4$, and 6 K. The saturated value of M, obtained at $T = 1.9$ K from an extrapolation of M vs $1/B$ to $1/B = 0$, is 0.75 μ_B for $Ce_3Rh_4Sn_{13}$ (sample #1), 0.98 μ_B for $Ce_3Rh_4Sn_{13}$ (sample #2), and 0.96 μ_B for $Ce_3Co_4Sn_{13}$.

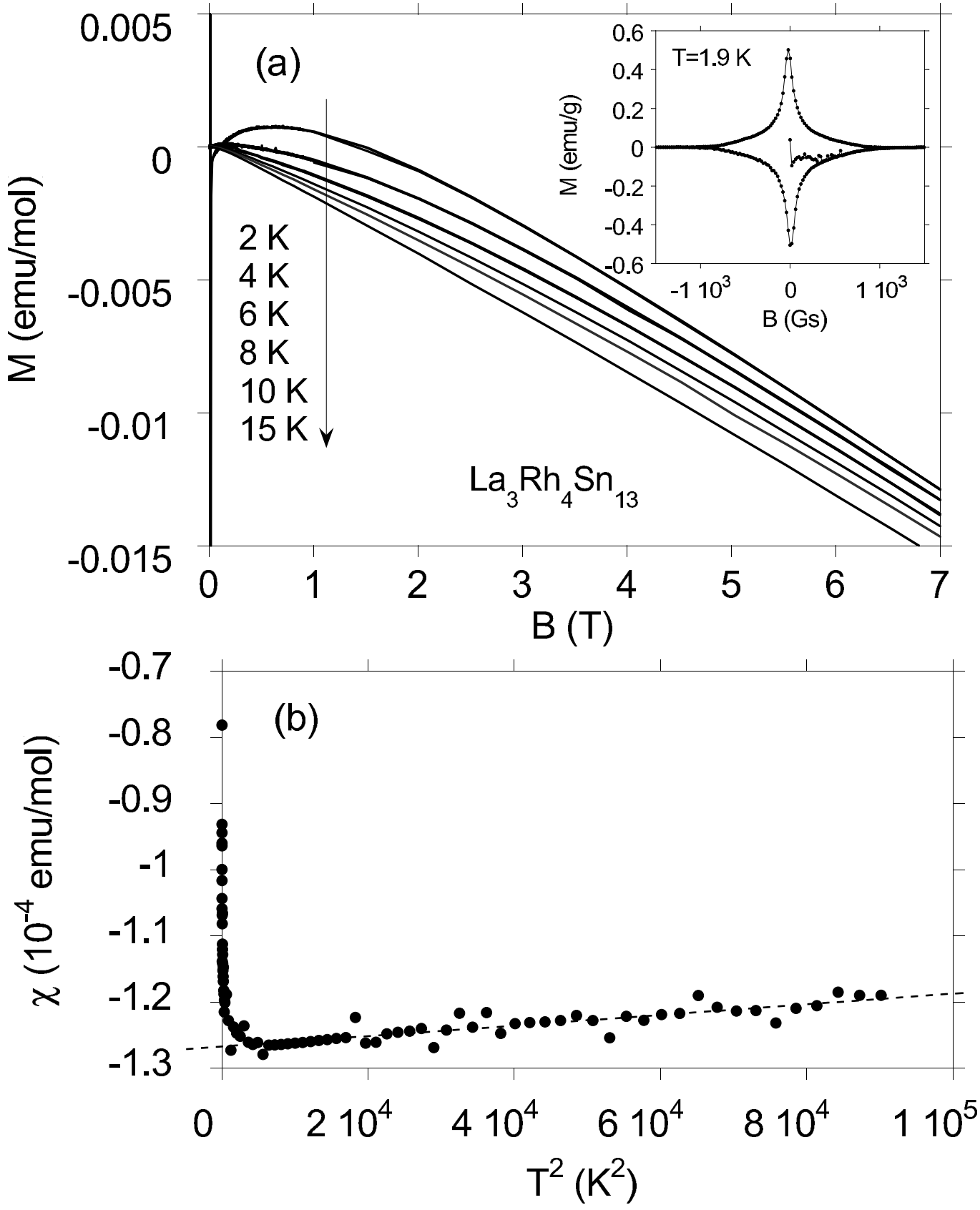
(a)
M (emu/mol)
B (T)
2 K
4 K
6 K
8 K
10 K
15 K
La3Rh4Sn13
T=1.9 K
M (emu/g)
B (Gs)
(b)
χ (10-4 emu/mol)
T2 (K2)

FIG. 5: (*a*) Magnetization M vs. magnetic field B measured at different temperatures for $La_3Rh_4Sn_{13}$. The inset shows a symmetric hysteresis loop at $T = 1.9$ K (in the superconducting state). Panel (*b*) displays the magnetic susceptibility for $La_3Rh_4Sn_{13}$ at the magnetic field $B = 1000$ Gs.

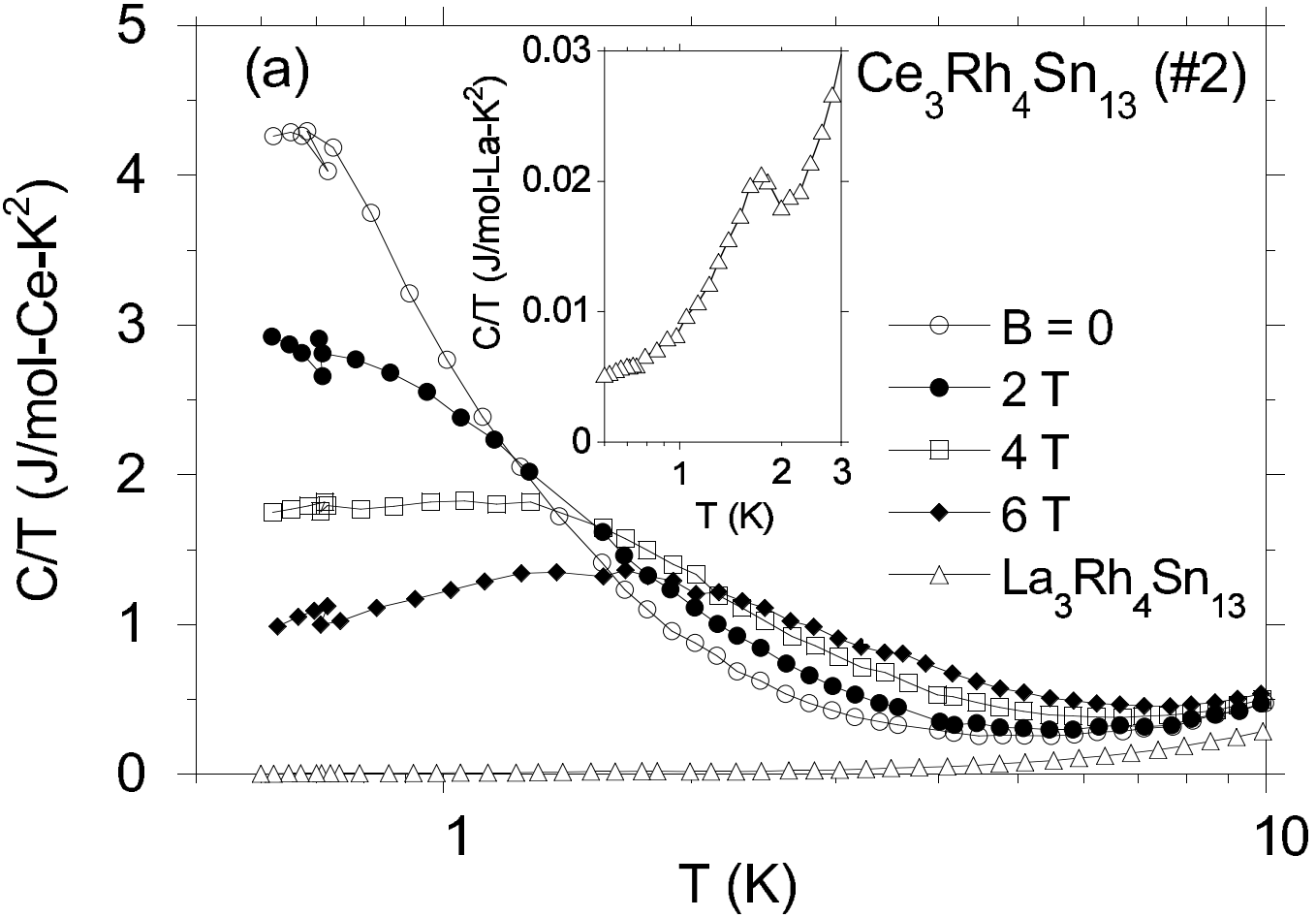
(a)
Ce3Rh4Sn13 (#2)
C/T (J/mol-Ce-K2)
T (K)
B = 0
2 T
4 T
6 T
La3Rh4Sn13
C/T (J/mol-La-K2)
T (K)

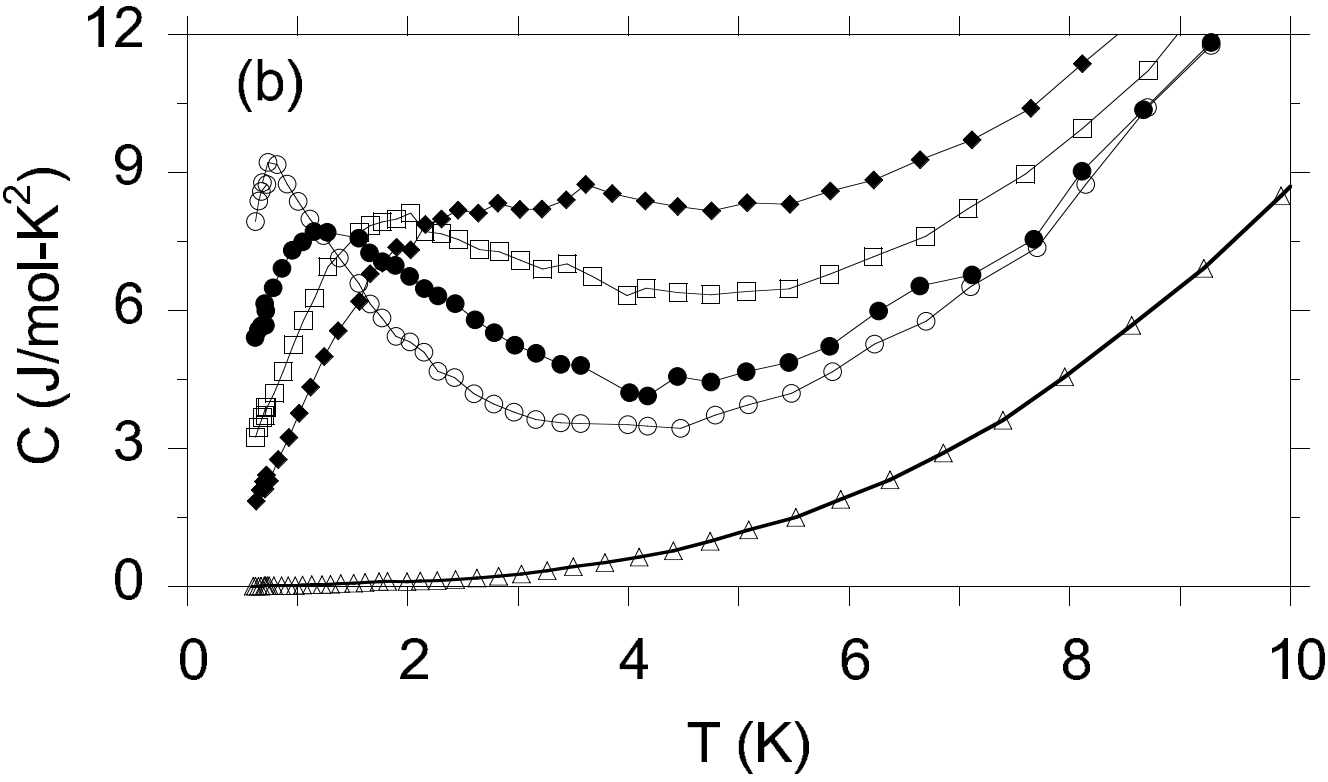
(b)
C (J/mol-K2)
T (K)

FIG. 6: $Ce_3Rh_4Sn_{13}$ (#2): $C(T)/T$ (in panel a) as a function of applied magnetic fields. The inset exhibits C/T low-T data for the reference compound $La_3Rh_4Sn_{13}$ near the critical temperature T_c. Panel b shows the specific heat C at different magnetic fields. The C/T and C data for $La_3Rh_4Sn_{13}$ is measured for $B = 0$.

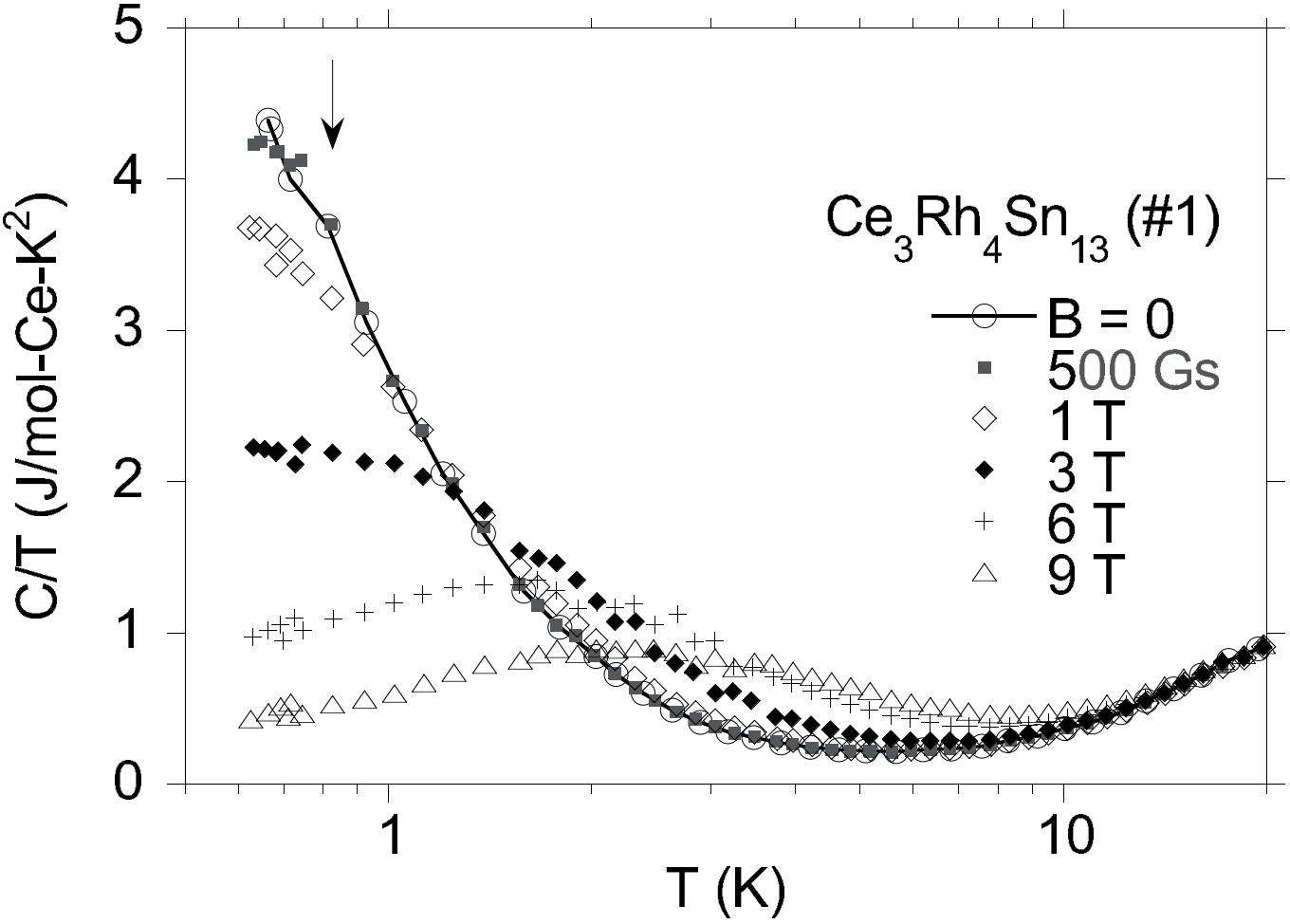

FIG. 7: $Ce_3Rh_4Sn_{13}$ (#1): $C(T)/T$ as a function of applied magnetic fields. The arrow signals atypical behavior which could result from the magnetic transition.

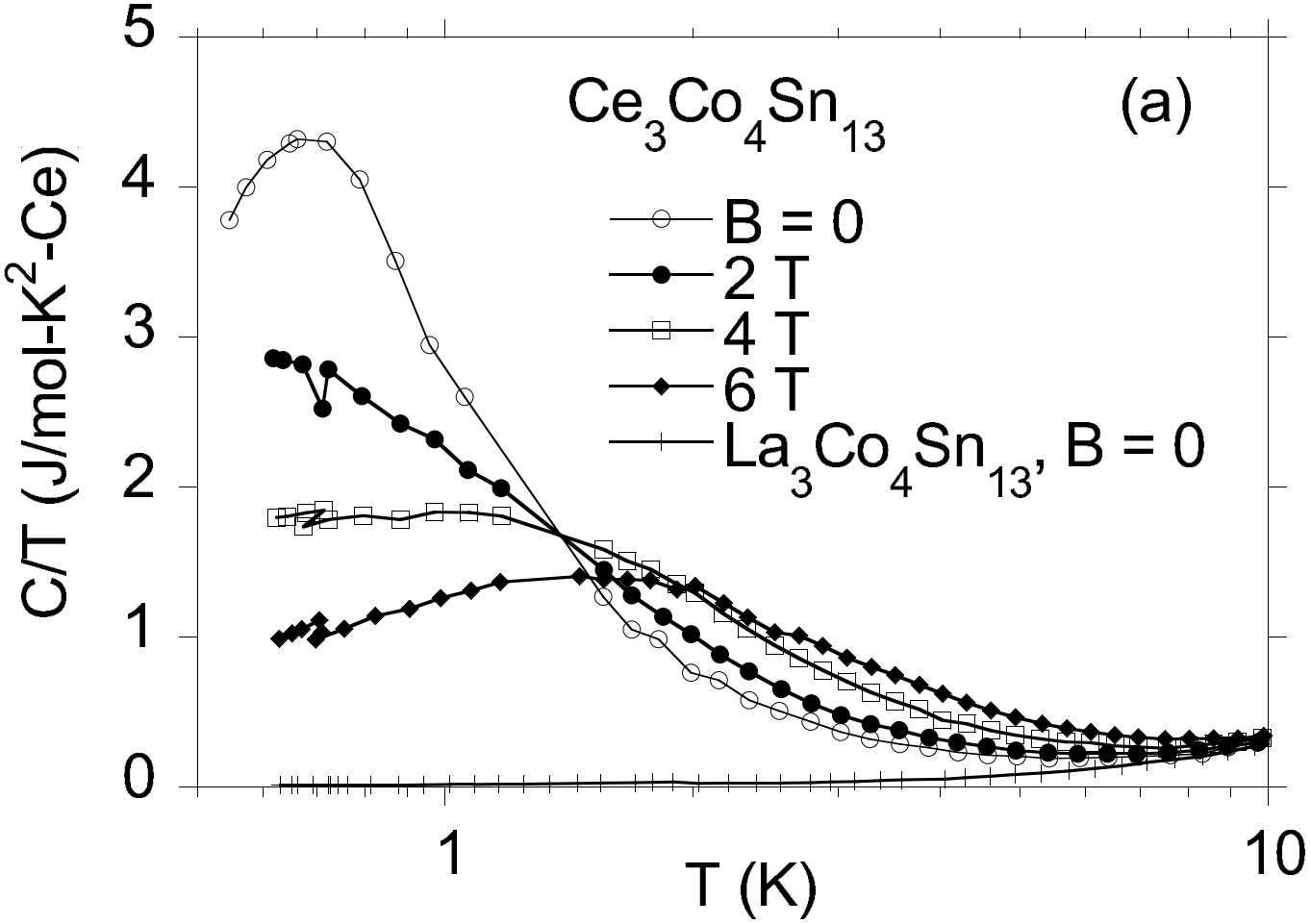
Ce3Co4Sn13
(a)
B = 0
2 T
4 T
6 T
La3Co4Sn13, B = 0
C/T (J/mol-K2-Ce)
T (K)
0
1
2
3
4
5
1
10

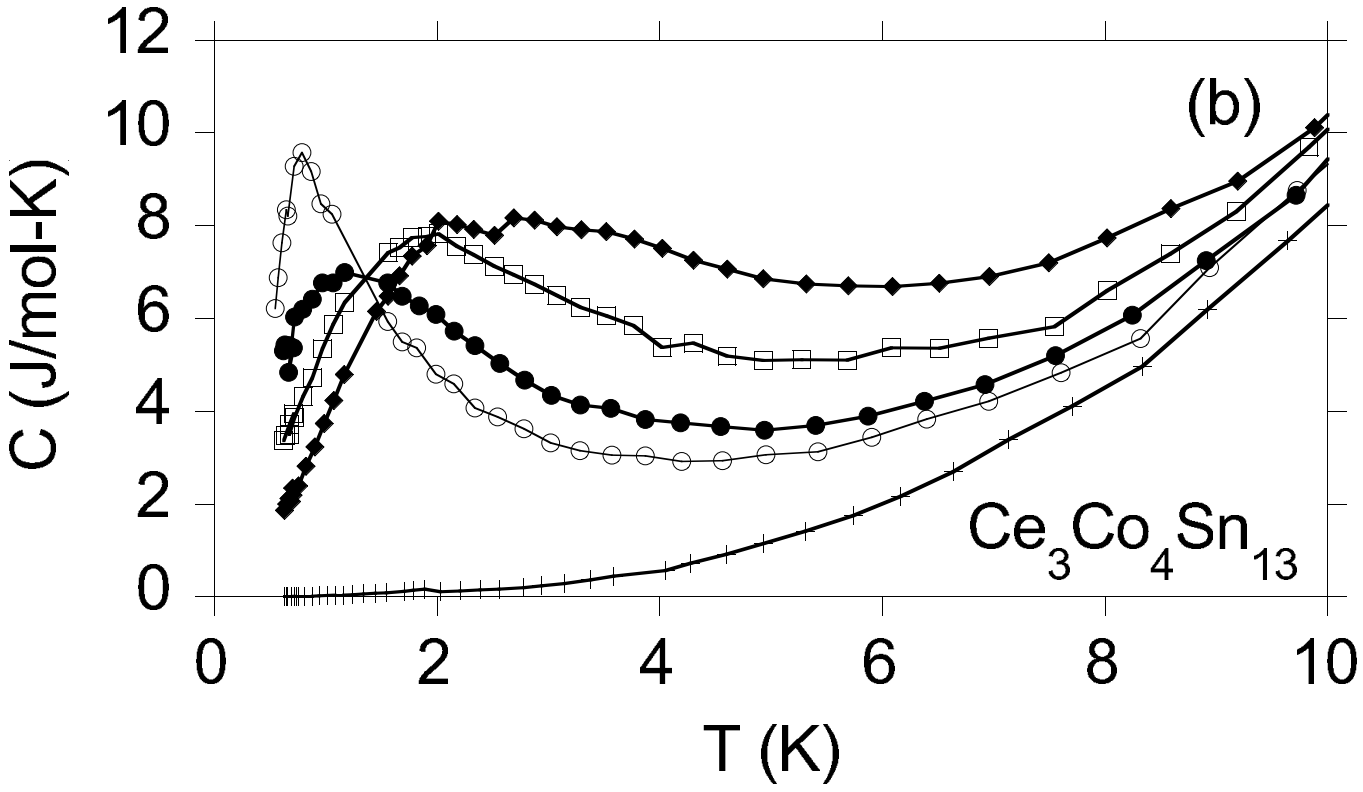
(b)
Ce3Co4Sn13
C (J/mol-K)
T (K)
0
2
4
6
8
10
12

FIG. 8: $Ce_3Co_4Sn_{13}$: $C(T)/T$ (panel a) as a function of temperature at various applied magnetic fields. Panel b shows the specific heat data, C, vs. T in the magnetic fields specified in panel a.

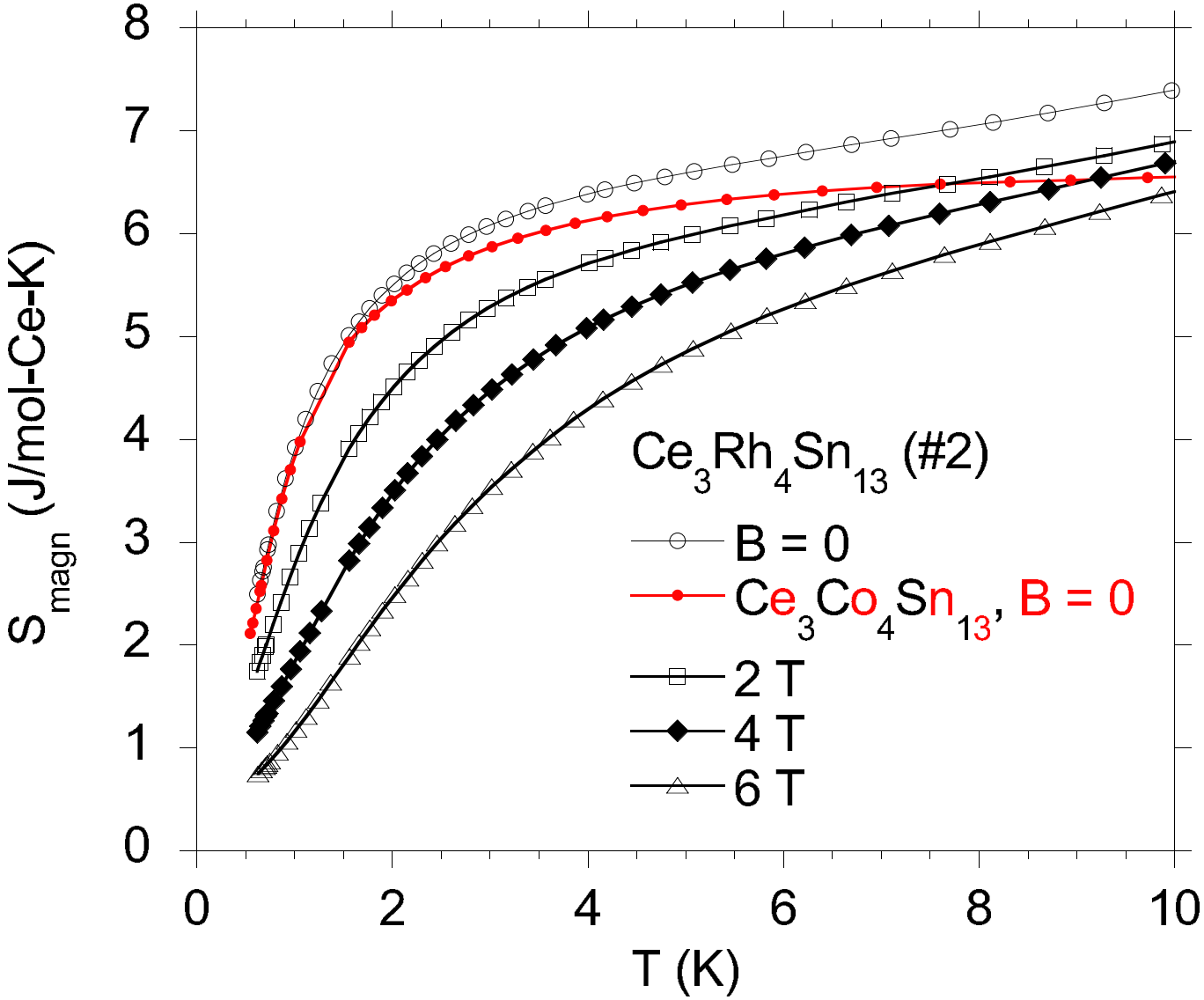

FIG. 9: The entropy S of the samples $Ce_3Rh_4Sn_{13}$ and $Ce_3Co_4Sn_{13}$ vs. temperature at different magnetic fields.

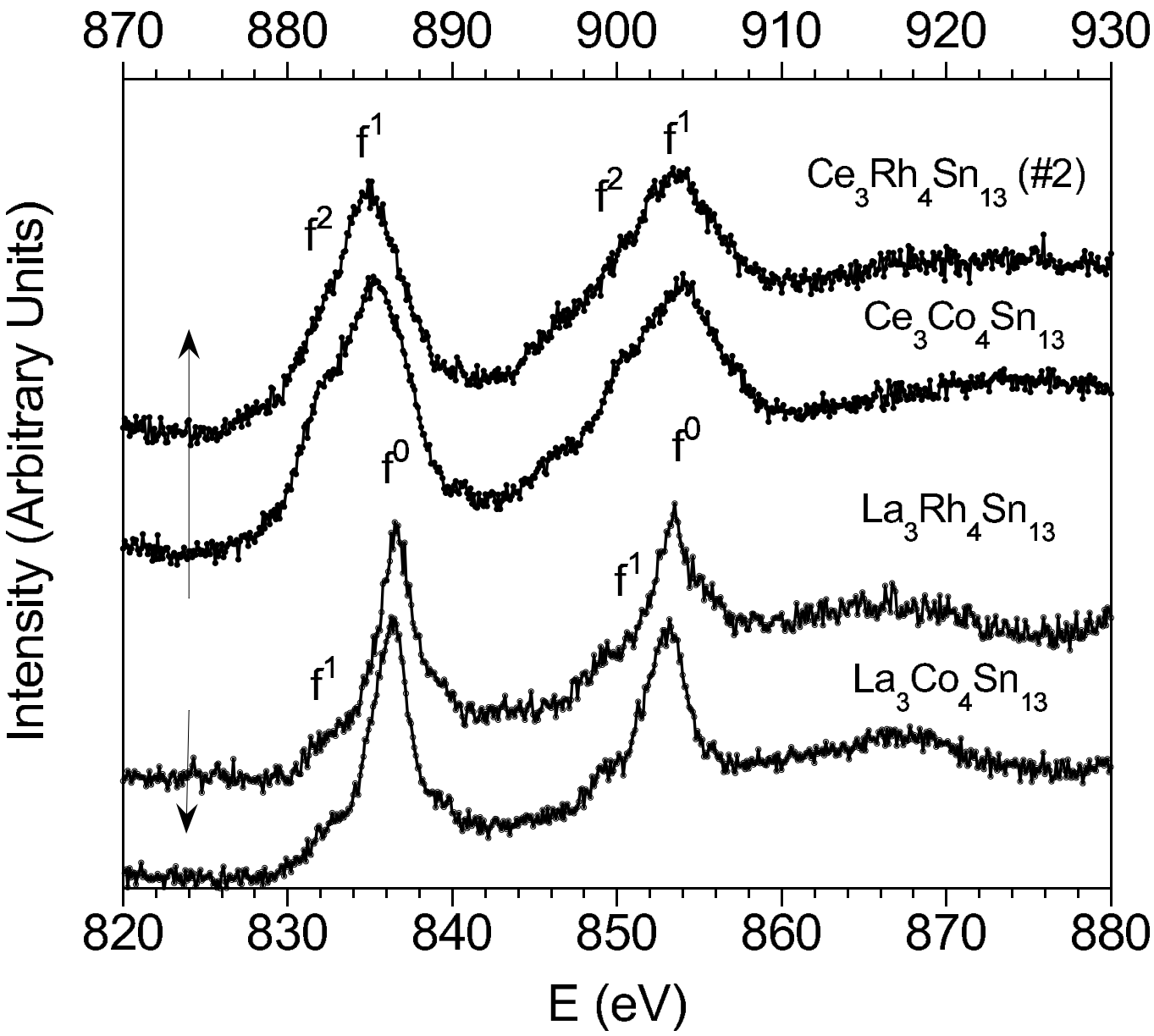

FIG. 10: The Ce $3d$ XPS spectra of $Ce_3M_4Sn_{13}$ and $La_3M_4Sn_{13}$, where M = Rh and Co with evidence for the $3d^9 4f^n$ components ($n = 1, 2$) for $Ce_3M_4Sn_{13}$, while $n = 0, 1$ in case of $La_3M_4Sn_{13}$.

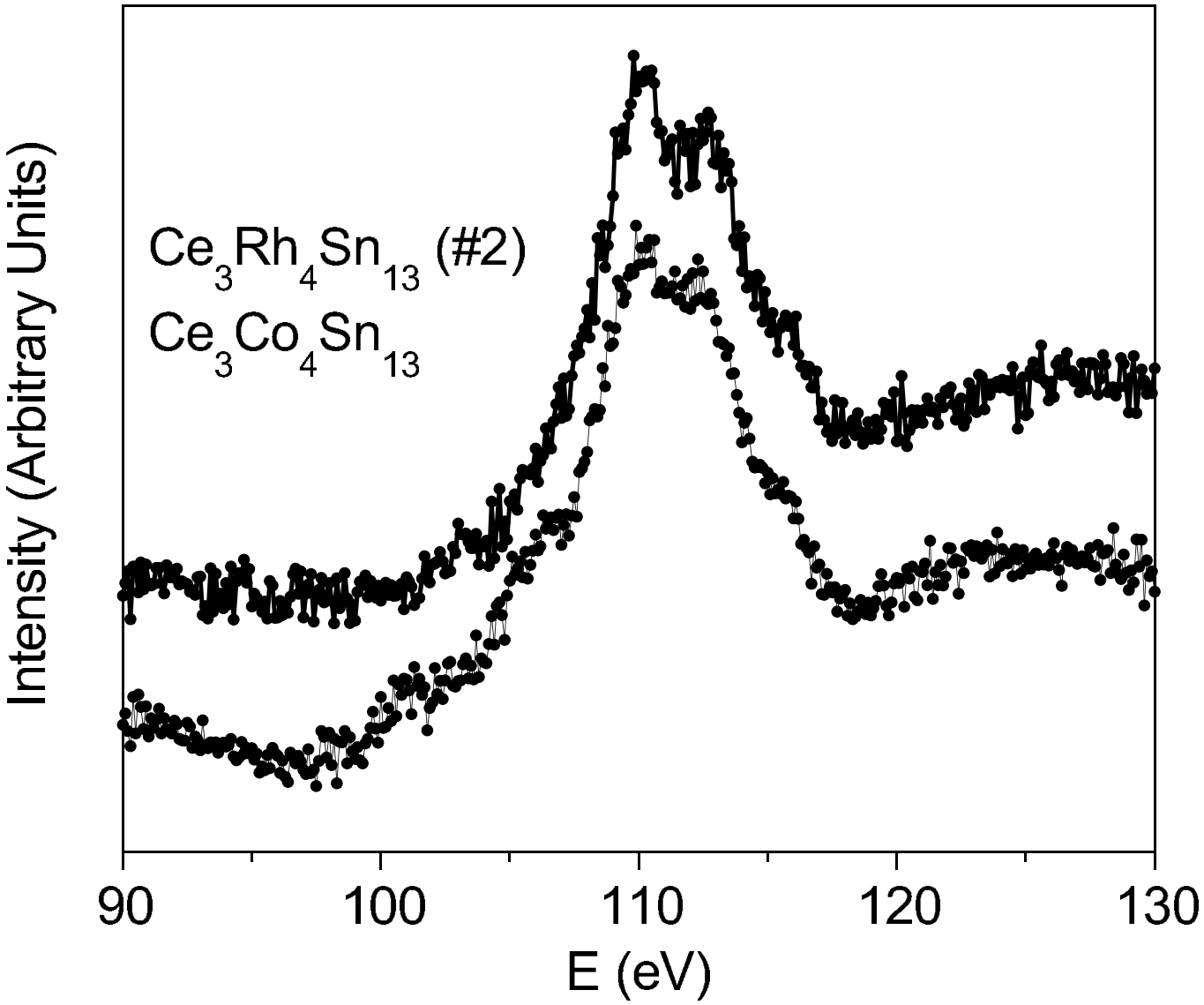

FIG. 11: The Ce 4*d* XPS spectra obtained for $Ce_3M_4Sn_{13}$, M = Rh or Co.

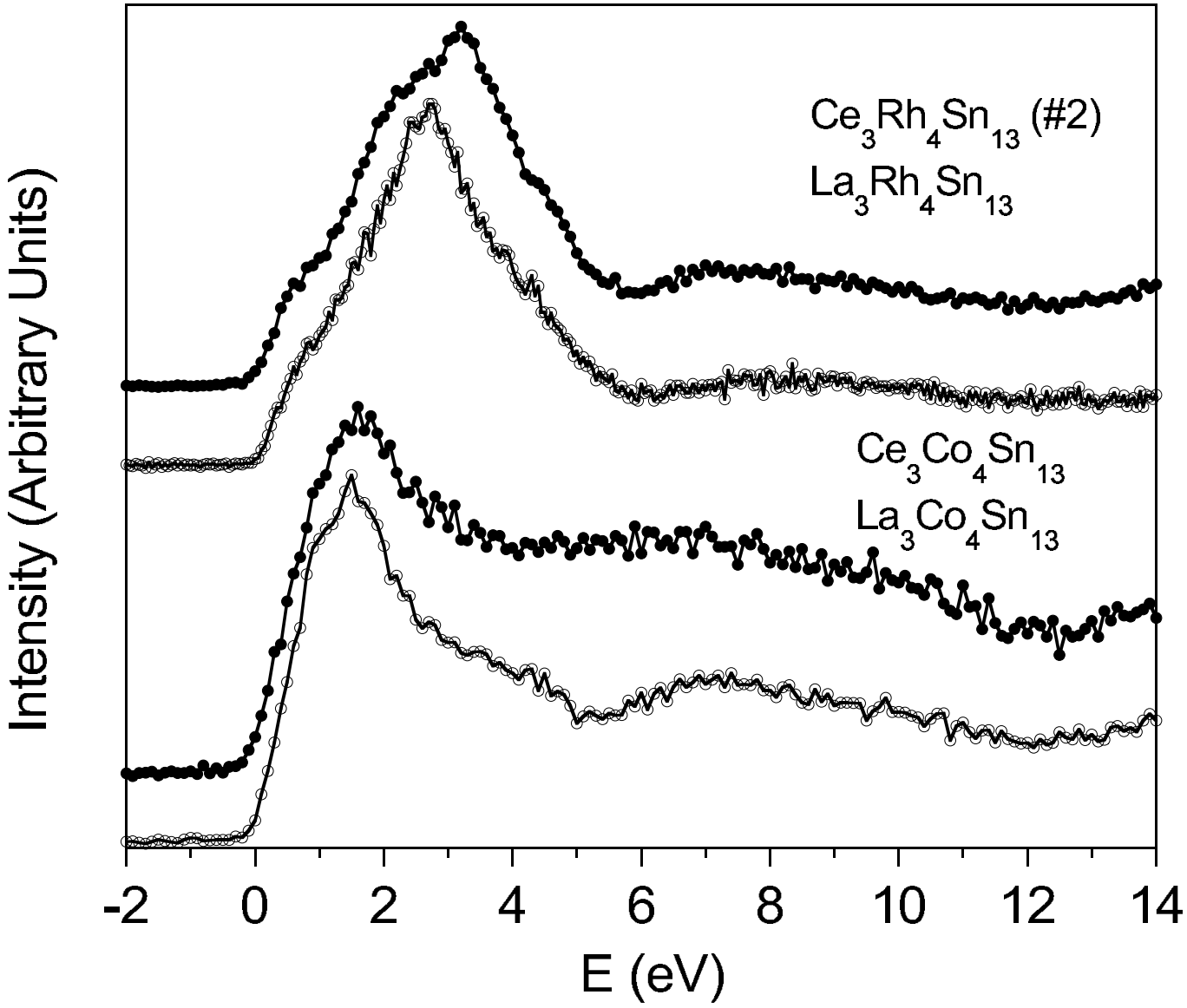

FIG. 12: The valence band XPS spectra measured for $Ce_3M_4Sn_{13}$ and $La_3M_4Sn_{13}$, where M = Rh or Co.

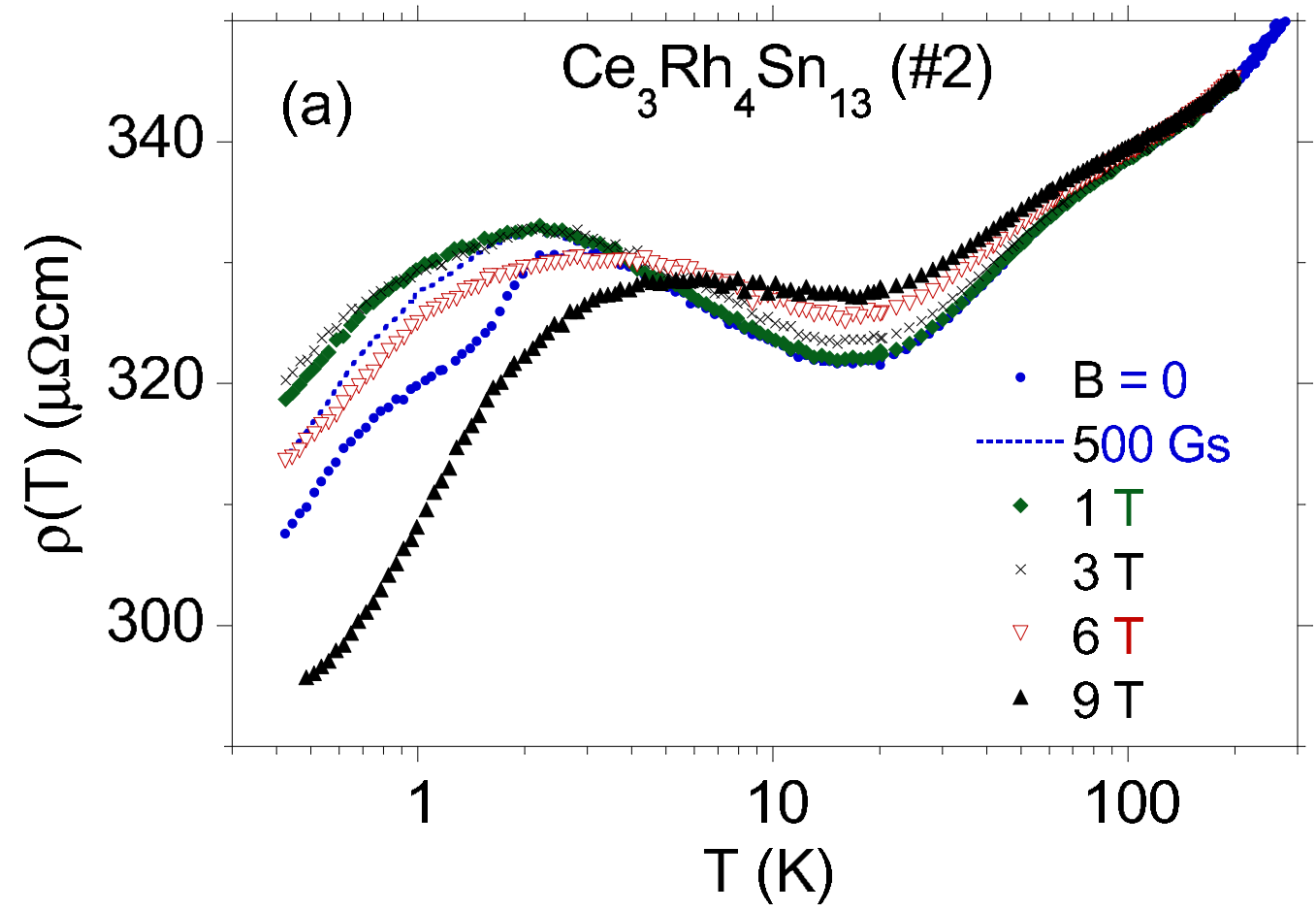
(a)
Ce3Rh4Sn13 (#2)
ρ(T) (μΩcm)
340
320
300
1
10
100
T (K)
B = 0
500 Gs
1 T
3 T
6 T
9 T

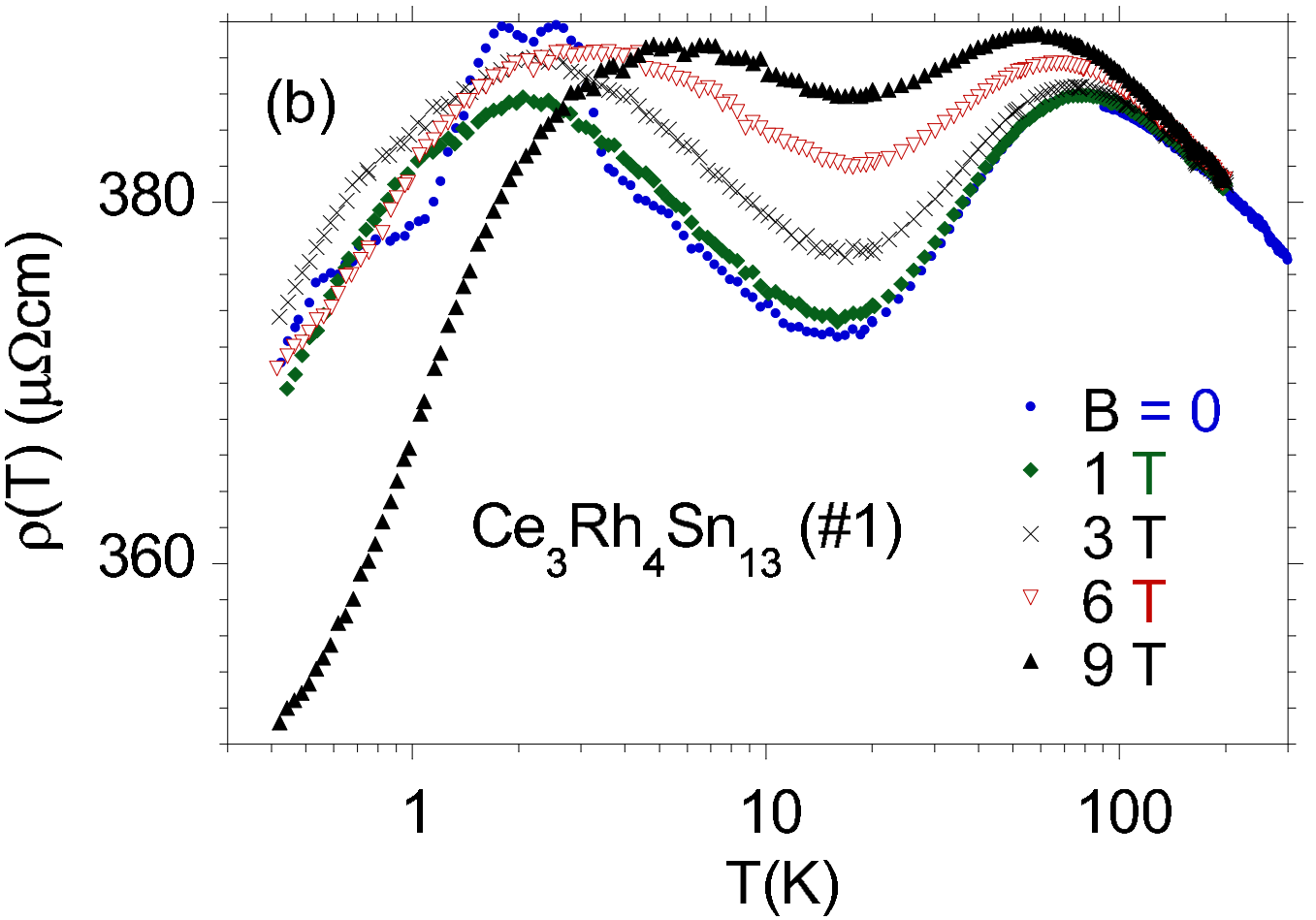
(b)
Ce3Rh4Sn13 (#1)
ρ(T) (μΩcm)
380
360
1
10
100
T(K)
B = 0
1 T
3 T
6 T
9 T

FIG. 13: Electrical resistivity at different magnetic fields for $Ce_3Rh_4Sn_{13}$; samples #1 and #2 are shown in panel *a* and *b*, respectively.

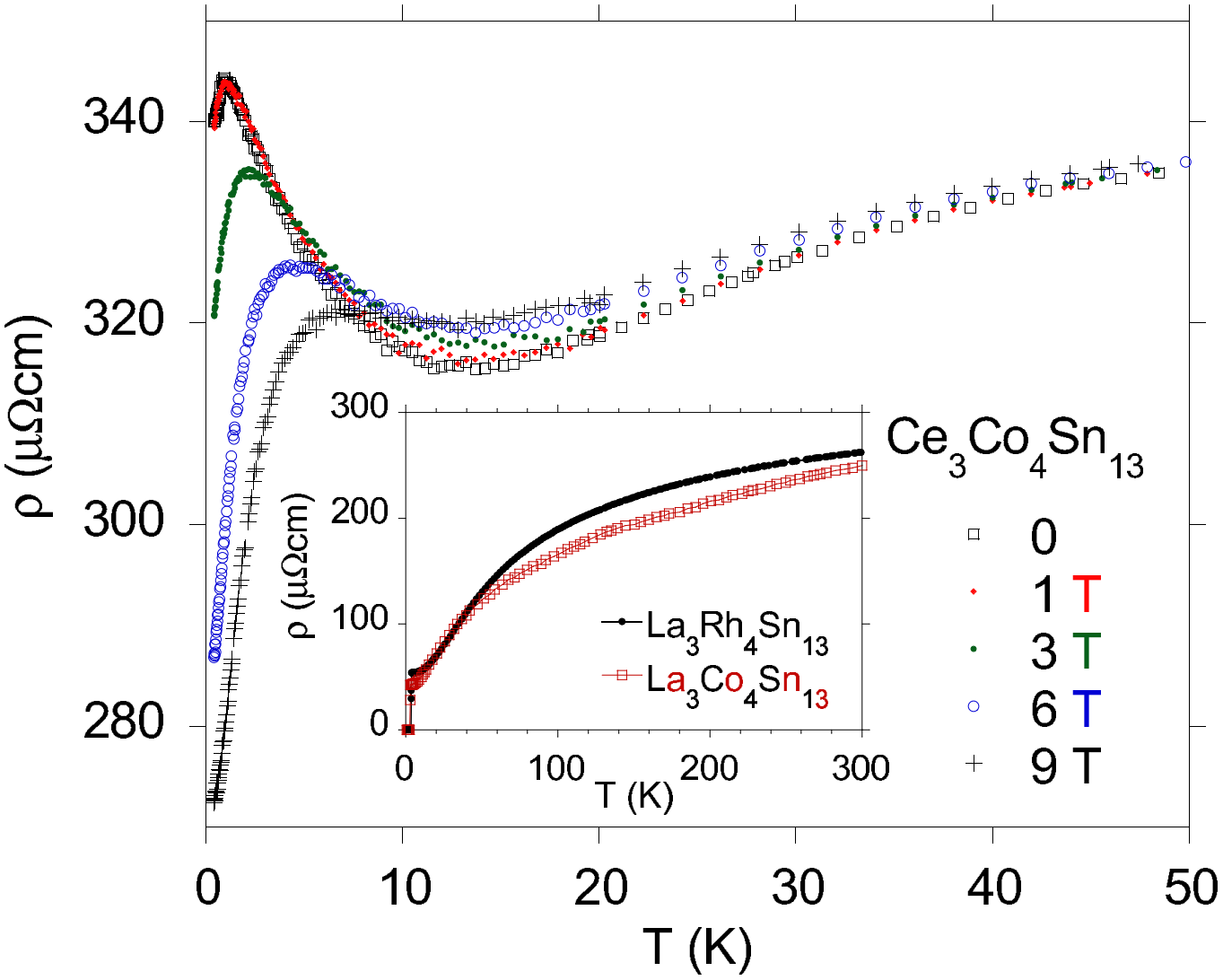

FIG. 14: Electrical resistivity at different magnetic fields for $Ce_3Co_4Sn_{13}$. The inset shows the resistivity of $La_3Rh_4Sn_{13}$ and $La_3Co_4Sn_{13}$.

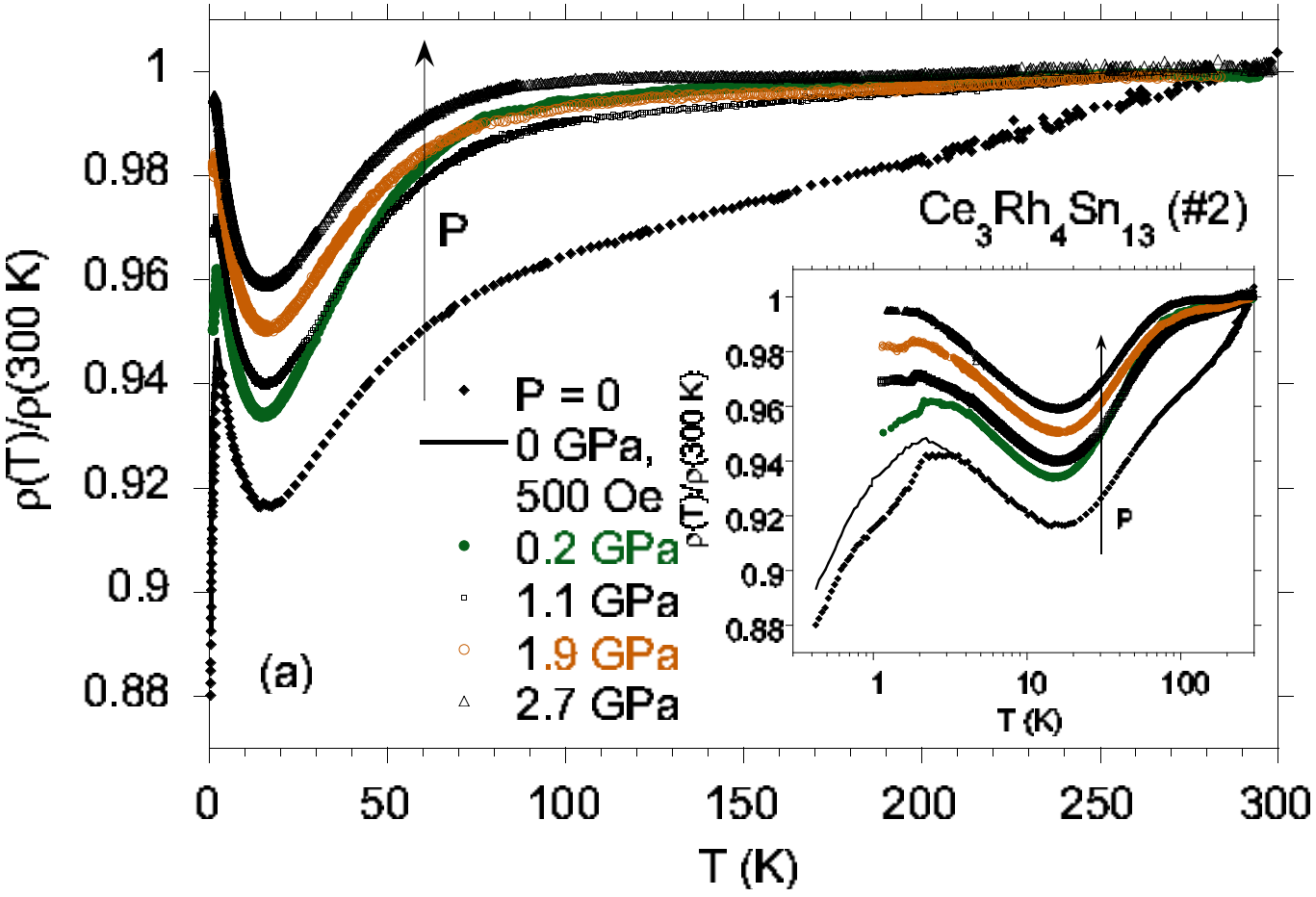
ρ(T)/ρ(300 K)
T (K)
P
Ce3Rh4Sn13 (#2)
P = 0
0 GPa, 500 Oe
0.2 GPa
1.1 GPa
1.9 GPa
2.7 GPa
(a)
T (K)

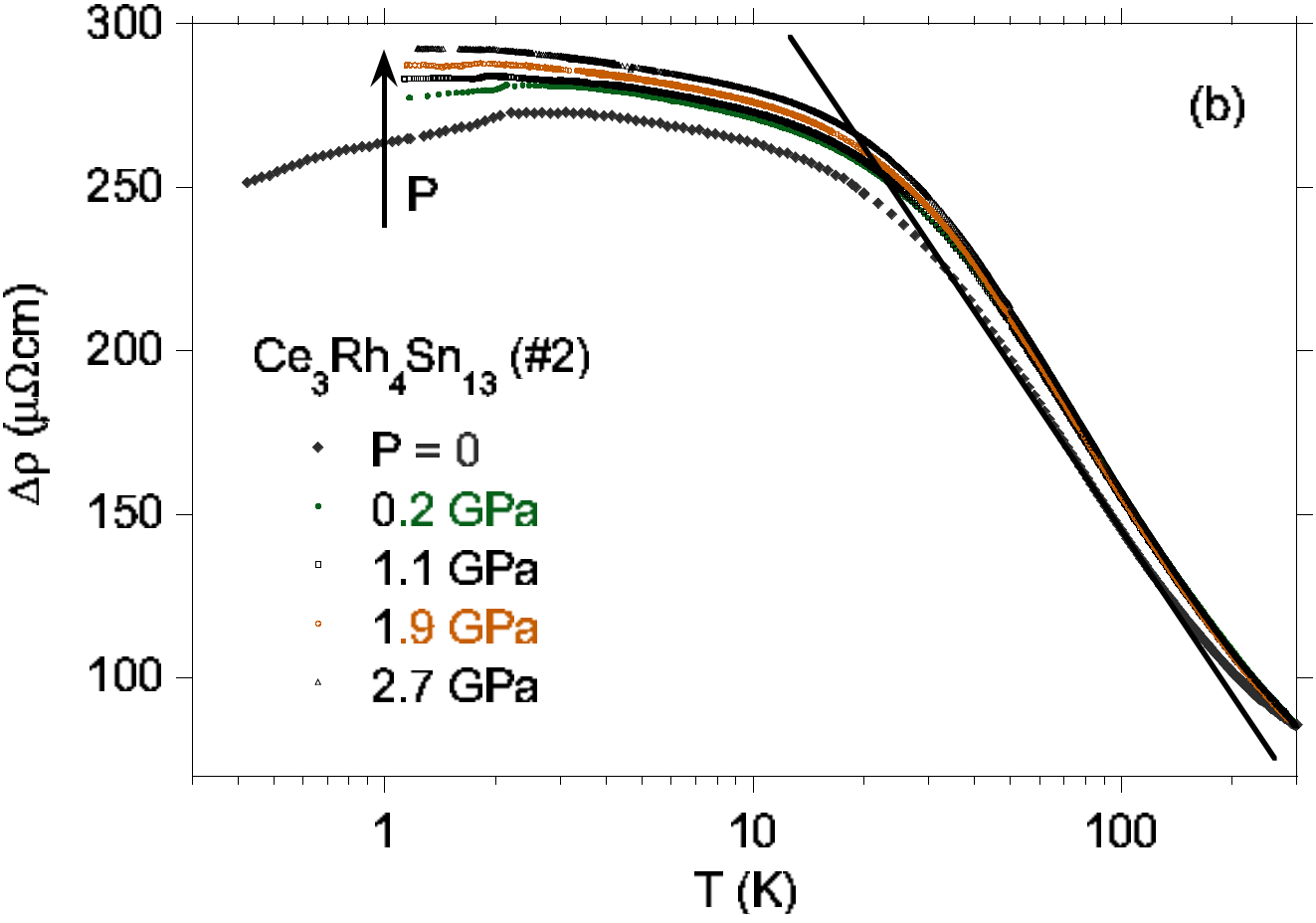
Δρ (μΩcm)
T (K)
P
(b)
Ce3Rh4Sn13 (#2)
P = 0
0.2 GPa
1.1 GPa
1.9 GPa
2.7 GPa

FIG. 15: Electrical resistivity for $Ce_3Rh_4Sn_{13}$ (#2) under applied pressure and normalized by the resistivity at $T = 300$ K (in panel a). The inset shows the ρ-data vs. $\log T$. Panel b shows $\Delta\rho$ vs $\log T$, where $\Delta\rho = \rho(Ce_3Rh_4Sn_{13}) - \rho(La_3Rh_4Sn_{13})$.

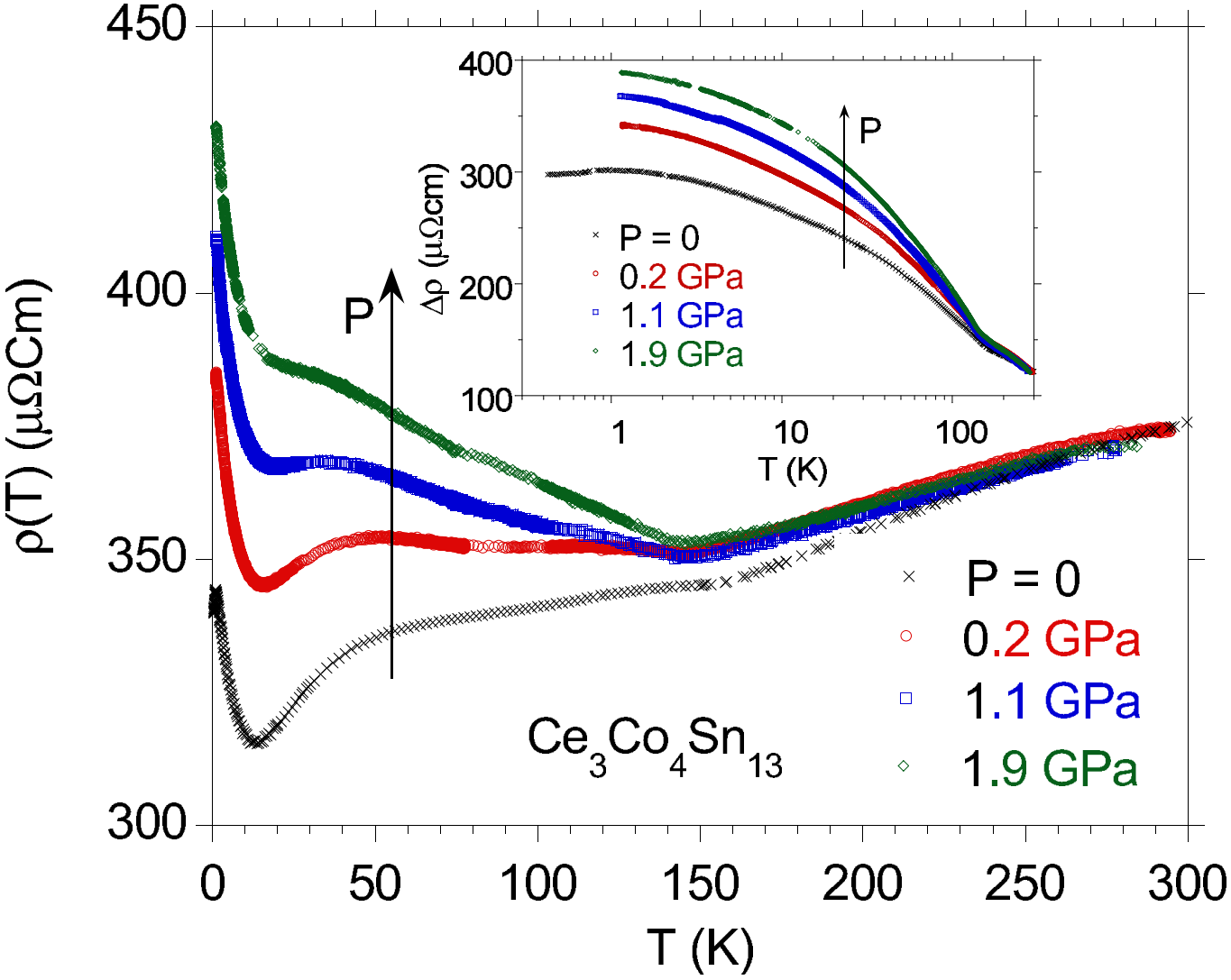

FIG. 16: Electrical resistivity for $Ce_3Co_4Sn_{13}$ under applied pressure. The inset shows the $\Delta\rho$-data vs. $\log T$, where $\Delta\rho = \rho(Ce_3Co_4Sn_{13}) - \rho(La_3Co_4Sn_{13})$.

Tables

TABLE I: Atomic distances and lattice parameters a (in Å) for $Ce_3Co_4Sn_{13}$ at $T = 300$ K, 120 K and 12 K, obtained from Rietveld analysis.

	293 K	120 K	12 K
a	9.6038	9.5738	9.5672
Sn2 ($24k$)			
x	0	0	0
y	0.2989(7)	0.3006(4)	0.3042(9)
z	0.1622(3)	0.1608(8)	0.1581(7)
$Sn1(Sn2)_{12}$	3.2667	3.2645	3.2810
$Ce(Sn2)_4$	3.2778	3.2827	3.3113
$Ce(Sn2)_8$	3.4524	3.4269	3.3936
$Co(Sn2)_6$	2.5877	2.5868	2.6004